MASTER'S THESIS ASSIGNMENT

I. Personal and study details

Student's name: **Prysiazhniuk Yeva** Personal ID number: **461438**

Faculty / Institute: **Faculty of Electrical Engineering**

Department / Institute: **Department of Computer Science**

Study program: **Medical Electronics and Bioinformatics**

Specialisation: **Bioinformatics**

II. Master's thesis details

Master's thesis title in English:

Measuring Arterial spin labeling MRI - calibration from M0-scans with background suppression

Master's thesis title in Czech:

Vyhodnocení Arterial spin labeling MRI – kalibrace z dat s potlačením pozadí

Guidelines:

Arterial spin labeling MRI is a non-invasive method for measuring brain perfusion using magnetically labeled water. To obtain absolute quantification, use of a so-called M0 calibration scan is necessary to establish the equilibrium blood magnetizaion. Under certain circumstances, this calibration M0-scan is acquired with reduced tissue signal called background suppression. Traditionally, such scans are used for relative quantification only or discarded. The goal of the project is to correct for the signal loss to allow full quantitative use of the data. Correction of the background suppression is, in theory, straightforward as the correction can be reconstructed from the timings and intensity of the background suppression pulses used in the acquisition. This kind of correction is part of the quantification routines implemented in the pipeline for processing ASL data called ExploreASL (Mutsaerts et al. 2020) . In practice, such a simple solution does not deliver satisfactory result as many other parameters comes to play such as efficiency of the suppression pulses, individual relaxation times, or the type of brain tissue. The goal of this project will be to establish the accuracy of the correction in different scenarios and propose a robust solution that takes into account the spatial position in the brain, To test and validate
this approach, a dataset of thirty volunteers of different ages will be used containing both standard calibration scans as well as scans with background suppresion, thus allowing a comparison with a gold-standard quantification. The student will
establish the accuracy of the calibration under different scenarios in different scan types – 2D EPI and 3D GRASE – with a different range of parameters, and propose a tailored solution for each of the scenarios to allow to choose the best approach
in clinical practice, where the standard calibration scans are not available.
The student is expected to perform a literature search on articles about background suppresion in ASL, analyze the currently used methods for background suppressed acquisition and summarize them in the thesis. Subsequently, the student will propose an optimal way for solving the problem and define a set of goals and requirements for the developed metho, and quantitative measures used to evaluate its performances.
The outcome of the project will be a report summarizing the usability of the method for different scanners, sequences, and brain regions as well as an implementation of the extension of the ExploreASL pipeline for use in clinical research.
The project will be supervised by Dr. J. Petr (Helmholtz-Zentrum Dresden-Rossendorf) and co-supervised by Dr. H. Mutsaerts (Amsterdam UMC) who will provide the access to data. The student will work with the ExploreASL software for the ASL data analysis and write custom Matlab scripts for the data evaluation.

Bibliography / sources:

[1] Alsop, David C., John A. Detre, Xavier Golay, Matthias Günther, Jeroen Hendrikse, Luis Hernandez-Garcia, Hanzhang Lu, et al. 2015. "Recommended Implementation of Arterial Spin-Labeled Perfusion MRI for Clinical Applications: A Consensus of the ISMRM Perfusion Study Group and the European Consortium for ASL in Dementia." Magnetic Resonance in Medicine: Official Journal of the Society of Magnetic Resonance in Medicine
/ Society of Magnetic Resonance in Medicine 73 (1): 102–16
[2] Garcia, Dairon M., Guillaume Duhamel, and David C. Alsop. 2005. "Efficiency of Inversion Pulses for Background Suppressed Arterial Spin Labeling." Magnetic Resonance in Medicine: Official Journal of the Society of Magnetic Resonance in Medicine / Society of Magnetic Resonance in Medicine 54 (2): 366–72
[3] Heijtel, D. F. R., H. J. M. M. Mutsaerts, E. Bakker, P. Schober, M. F. Stevens, E. T. Petersen, B. N. M. van Berckel, et al. 2014. "Accuracy and Precision of Pseudo-Continuous Arterial Spin Labeling Perfusion during Baseline and Hypercapnia: A Head-to-Head Comparison with 15O H2O Positron Emission Tomography."NeuroImage 92 (-): 182–92

[4] Hernandez-Garcia, Luis, Anish Lahiri, and Jonas Schollenberger. 2018. “Recent Progress in ASL.” NeuroImage, no. December 2017 (January): 1–14
[5] Mutsaerts, Henk J. M. M., Jan Petr, Paul Groot, Pieter Vandemaele, Silvia Ingala, Andrew D. Robertson, Lena Václavů, et al. 2020. “ExploreASL: An Image Processing Pipeline for Multi-Center ASL Perfusion MRI Studies.” NeuroImage, June, 117031
[6] Williams, D. S., J. A. Detre, J. S. Leigh, and A. P. Koretsky. 1992. “Magnetic Resonance Imaging of Perfusion Using Spin Inversion of Arterial Water.” Proceedings of the National Academy of Sciences of the United States of America 89 (1): 212–16

Name and workplace of master’s thesis supervisor:

Mgr. Jan Petr, Ph.D., Helmholtz-Zentrum Dresden-Rossendorf

Name and workplace of second master’s thesis supervisor or consultant:

Date of master’s thesis assignment: **11.02.2021** Deadline for master's thesis submission: **21.05.2021**

Assignment valid until: **30.09.2022**

Mgr. Jan Petr, Ph.D. Supervisor’s signature	Head of department’s signature	prof. Mgr. Petr Páta, Ph.D. Dean’s signature

III. Assignment receipt

The student acknowledges that the master’s thesis is an individual work. The student must produce her thesis without the assistance of others, with the exception of provided consultations. Within the master’s thesis, the author must state the names of consultants and include a list of references.

.	
Date of assignment receipt	Student’s signature

Czech Technical University
Faculty of Electrical Engineering
Department of Computer Science

Measuring Arterial spin labeling MRI - calibration from M0-scans with background suppression

Yeva Prysiazhniuk

Master's program: Medical Electronics and Bioinformatics
Specialization: Bioinformatics
Supervisor: Mgr. Jan Petr, Ph.D.

Prague, May 2021

Supervisor:
Mgr. Jan Petr, Ph.D.
Institute of Radiopharmaceutical Cancer Research
Helmholtz-Zentrum Dresden-Rossendorf
Bautzner Landstrasse 400
01328 Dresden
Germany

Declaration

I hereby declare I have written this master thesis independently and quoted all the sources of information used in accordance with methodological instructions on ethical principles for writing an academic thesis. Moreover, I state that this thesis has neither been submitted nor accepted for any other degree.

Prague, 2021

.....
Yeva Prysiazhniuk

Abstract

Keywords:
ASL MRI, perfusion imaging, brain imaging, ExploreASL, M0 calibration.

Arterial spin labeling (ASL) is a method for magnetic resonance imaging (MRI) that allows to measure brain perfusion non-invasively using magnetically labeled water instead of using radioactive tracers or contrast agents. To obtain absolute quantification, the value of equilibrium magnetization in arterial blood needs to be obtained in every patient. This is usually done with the use of a so-called M0 scan that can be rapidly obtained along with the ASL measurement. Despite the acquisition of an M0-scan is recommended in the majority of literature, it is not always available in practice. This work proposes a novel approach of M0-scan estimation from the ASL scans despite that the static-tissue signal is actively suppressed there. Two different approaches are implemented and tested - a simple single-tissue model, and an advanced model that assumes mixing of signal of multiple tissues with different relaxation properties. The methods were tested on real MRI data (2D EPI and 3D GraSE readouts) acquired in five healthy volunteer in terms of accuracy and inter-session intra-subject reproducibility in M0 estimation and subsequent perfusion quantification. This work lays ground for potential use in clinical practice, though further testing in larger population is needed to establish the performance in a wider spectrum in image acquisitions settings.

Klíčová slova:
ASL MRI, perfuzní zobrazování, neurozobrazování, ExploreASL, M0 kalibrace.

Arterial spin labeling (ASL) je metoda pro zobrazování magnetickou rezonancí (MRI), která umožňuje měřit prokrvení mozku neinvazivně pomocí magneticky označené vody namísto použití radioaktivních indikátorů nebo kontrastních látek. K získání absolutní kvantifikace je třeba u každého pacienta získat hodnotu rovnovážné magnetizace v arteriální krvi. To se obvykle provádí pomocí takzvaného M0 skenu, které lze rychle získat spolu s měřením ASL. Navzdory tomu, že je použití M0 skenu doporučeno ve většině literatury, není M0 sken v praxi vždy k dispozici. Tato práce navrhuje nový přístup k rekonstrukci M0 skenů z ASL skenů, přestože v nich je statický signál z tkání aktivně potlačen. Byly naimplementovány a otestovány dvě různé metody - jednoduchý model pracující s jedním typem tkáně a pokročilý model, který předpokládá směs signálu z více různých typů tkání s různými relaxačními vlastnostmi. Obě metody byly otestovány na reálných MRI datech (ze sekvencí 2D EPI a 3D GraSE) naměřených v pěti zdravých dobrovolnících a porovnány z hlediska přesnosti a reprodukovatelnosti opakovaných měřeních jak při odhadu M0-skenu, tak při jeho zapojení do kvantifikace prokrvení. Tato práce připravuje základy pro potenciální použití v klinické praxi, ačkoli k prokázání efektivity algoritmu při použití v širším spektru různě nastavených MRI sekvencí je zapotřebí dalšího testování ve větší populaci.

Acknowledgements

I want to express my gratitude to Dr. Jan Petr for his great dedication, guidance, and invaluable advice that inspired me to study ASL imaging and helped me to complete this work. I am thankful to Dr. Kim van de Ven and Dr. Koen Baas for providing us with data, which became the essential foundation of this work, and for reviewing the thesis. I thank Dr. Yuriko Suzuki and OSIPI TF4.1 for providing useful diagrams and standard notation that helped me navigate in the ASL imaging terminology. I would also like to thank Mathijs Dijsselhof, Dr. Henk-Jan Mutsaerts, Dr. Aaron Oliver-Taylor, and Dr. David Thomas for reviewing the thesis and giving brilliant comments. My appreciation goes to Prof. Jan Kybic for reviewing the thesis and helping me with the opportunity to work on such research. Finally, I would like to thank my family for never-ending optimism and support.

Contents

List of Figures

List of Tables

Abbreviations

ASL	Arterial spin labeling
BS	Background suppression
CBF	Cerebral blood flow
CSF	Cerebrospinal fluid
CT	Computed tomography
DCE	Dynamic contrast-enhanced
DSC	Dynamic susceptibility contrast
EPI	Echo planar imaging
GBCA	Gadolinium-based contrast agent
GM	Gray matter
GraSE	Gradient spin echo
MB	Multiband
MRE	Mean relative error
MRI	Magnetic resonance imaging
PASL	Pulsed arterial spin labeling
pCASL	Pseudo-continuous arterial spin labeling
PET	Positron emission tomography
PLD	Post-labeling delay
PVC	Partial volume correction
PVE	Partial volume effect
RF	Radiofrequency
ROI	Region of interest
SNR	Signal-to-noise ratio
SPECT	Single-photon emission computerized tomography
TR	Repetition time
WM	White matter
WS RMSE	Within-subject root-mean-square error

Chapter 1

Introduction

1.1 Perfusion imaging

Perfusion refers to fluid passage, blood in this work, through the circulatory or lymphatic system to an organ or tissue. Poor perfusion can lead to serious clinical conditions, such as angina pectoris or ischemic stroke, whereas increased perfusion can signify inflammatory processes or generation of new tissue as in cancer. Perfusion imaging of blood passage through organs and tissues is currently gaining attention in clinical diagnostics and research applications. Perfusion imaging can identify issues with the decreased blood supply, restricted blood flow due to the changes in the blood vessels, physiological changes, and abnormalities; it is closely correlated with the metabolism in the tissues and electrical activity in the brain [1] [2]. The organs of the highest interest for perfusion imaging are the brain and the heart [3], though renal [4], liver [5], human eye [6], and prostate [7] perfusion imaging techniques are currently under active research and development. Particularly, cerebral perfusion imaging commonly focuses on measuring cerebral blood flow (CBF). Alterations in CBF are closely related to many brain disorders [8] and, therefore, they are of particular interest in neuroscience. Perfusion is an important parameter in studies and diagnostics of age-related changes in the brain [9], neurodegenerative diseases [10] [11] [12], neurovascular diseases [13], multiple sclerosis [14], brain tumors [15], traumatic brain injury [16], psychiatric disorders [17] [18] [19], etc.

There are multiple ways to image perfusion, including methods of computed tomography (CT), positron emission tomography (PET), single-photon emission computerized tomography (SPECT), ultrasound, and magnetic resonance imaging (MRI). MRI have several advantages compared to the other modalities. Unlike CT, SPECT, and PET, MRI does not lead to radiation exposure. Also, MRI provides more extensive application than ultrasound with its tissue and depth limitations.

There are two different approaches for measuring perfusion with MRI: based on the administration of a contrast-enhancing agent and without it. The first category includes dynamic susceptibility contrast (DSC) MRI and dynamic contrast-enhanced (DCE) MRI. Both DSC and DCE rely on the intravascular administration of the contrast-enhancing

agent, most commonly a gadolinium-based compound (GBCA). The penetration of these agents to the tissue is proportional to the blood flow rate, whereas their accumulation might indicate barrier disruption or tissue damage. DSC perfusion MR signal measures signal drops due to the shortening of T2* time caused by increased magnetic susceptibility of the passing GBCA. DCE measures signal increase due to the shortening of the T1-time due to the presence of GBCA. The major disadvantage of the GBCA-based techniques is the potential toxicity of gadolinium in patients with impaired renal function and in children. Also, linear-chelated GBCAs are known to accumulate in the brain after repeated administration and are a potential source of neural toxicity [21].

A completely non-invasive alternative is arterial spin labeling (ASL) MRI. ASL is based on the endogenous labeling of arterial blood without a need for externally administered contrast-enhancing agents. Its key principle lies in the magnetic labeling of the blood by the inversing the longitudinal magnetization. Then, the labeled blood travels through the macrovasculature and enters an organ or tissue. Consequently, the labeled blood exchanges with the tissue and thus decreases its longitudinal magnetization. This affects the measured signal in an image, called labeled image, which is taken after such labeling. A second image, called control image, is then obtained without such prior labeling. The difference between the control and the labeled images is then proportional to the amount of inflowing labeled blood and can be used for perfusion imaging. ASL MRI is the only non-invasive and cost-effective method that provides whole brain perfusion imaging in high resolution [22]. This makes this technique of high interest in both research and clinical practice.

ASL has a further advantage of being able to provide an absolute quantification of blood perfusion. For that purpose, the equilibrium blood magnetization has to be estimated to calibrate the measurement. Blood equilibrium magnetization is typically obtained from a so-called M0-calibration scan. This M0 scan is acquired with the same readout sequence

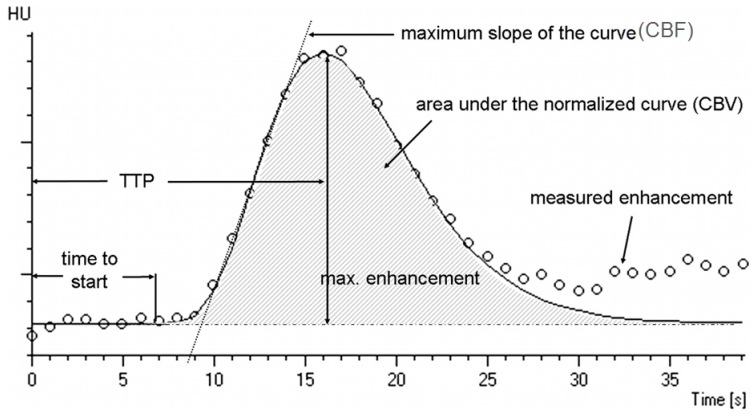

Figure 1.1: Time attenuation curve for the perfusion CT
The graph shows the time attenuation curve for the perfusion CT imaging [20]. Here we can see well-defined TTP and CBV. CBF is estimated as the maximum slope of the curve. MMT is equal to the ratio of CBV to CBF.

as labeled and control images with two main approaches: a long repetition time (TR) calibration scan, which provides signal closer to the true equilibrium magnetization, or a short TR calibration scan, which reduces the contrast between white and gray matter [23]. However, to improve the signal-to-noise ratio (SNR), ASL is now routinely acquired with background suppression (BS) pulses that suppress the signal from static tissue and related noise, effectively prohibiting the estimation of blood M0 from the control scans with background suppression. For this reason, M0-scan acquisition should be an integral part of all ASL protocols. However, in practice, many clinical studies do not acquire the necessary M0 scan because it was not implemented in the current version of software, was omitted in the protocol, or lost during data handling. Such studies have important issues with absolute CBF quantification if background suppression was used in the ASL data. In theory, the background suppression can be reverted in post-processing, thus opening the way for use of control images for the estimation of blood M0 and correct CBF quantification. However, currently, there is no established method to deal with this issue, and the limitations, reproducibility, and accuracy of such M0 estimation from the control scans with BS are not known.

The goal of this thesis is to correct for the signal loss in control images with BS to allow its use as an M0 scan. First of all, this work comprises the literature research on background suppression in ASL and the currently used methods for background suppressed acquisition. The experimental part of the thesis includes the implementation of the methods to estimate M0 scans from control images. The accuracy of the method is established for two different readout sequences – 2D EPI and 3D GraSE. Also, the performance of the method for CBF quantification is tested and compared with a reference approach using a measured M0-scan, and the accuracy and reproducibility of the proposed methods across scanning sessions is assessed. Finally, the optimal way for solving the issue with CBF quantification without M0-image is proposed.

1.2 Structure of the Thesis

The thesis is organized into 5 chapters as follows:

1. *Introduction*: Here, the basic definitions of perfusion imaging and goals of the thesis are given

2. *Background Knowledge*: This chapter gets the reader into the topic of ASL MRI imaging from the theoretical perspective and explains relevant concepts in MRI image acquisition. A specific focus is put on the labeling and readout sequences, background suppression, and image processing.

3. *Methods*: This part describes the experimental part of the thesis; specifically, it outlines the data, the methods, and the evaluation done in the scope of this work.

4. *Results*: The chapter reports the outcomes of the experimental part.

5. *Discussion*: The chapter gives an overview of the work conducted within the thesis, interprets the findings, defines future work, and concludes the work.

Chapter 2

Background Knowledge

2.1 Arterial Spin Labeling MRI

ASL MRI provides quantitative measurement of CBF using a selective radiofrequency (RF) pulse to excite a bolus of blood inside an artery before entering an organ or tissue. The blood is labeled by inverting the magnetization of hydrogen atoms in blood water by a 180° pulse. The labeled atoms are then used as endogenous diffusible tracers. After a certain time interval, called post-labeling delay (PLD), the labeled particles arrive in the region of interest (ROI) and exchange with the tissue, thus decreasing its magnetization. At this moment, an image of the ROI is acquired with its intensity affected by the amount of labeled blood that perfused the tissue. The exact location of labeling pulse and the duration of the time interval between labeling and scanning depend on the choice of the labeling approach described in the Section 2.2. A second image, called the control image, is then acquired without prior labeling, which does not contain labeled particles. Multiple pairs of control-labeled images are acquired and are consequently substracted to produce the perfusion-weighted image. The intensities in the perfusion-weighted image reflect the amount of labeled blood in each voxel and are directly proportional to the perfusion. However, to quantify the perfusion, the equilibrium magnetization of blood needs to be obtained for calibration. This is usually done using an M0-image that is acquired without prior labeling and has signal directly proportional to the voxel water content [24].

The produced ASL perfusion signal in a single control-label difference image is around 1% of the signal in the original control images [25], [26]. Since the signal is so low, the SNR of a single difference is very low and repeated measurements are required to reach reasonable quality of CBF maps. Since the initial introduction of the technique, important modifications of the methodology and hardware were established, such as prolonging the post-labeling delay [27], background suppression [28] [29], and new labeling techniques (as pseudo-continuous labeling [30]), to suppress the noise and induce the signal [31]. Labeling approaches and background suppression (BS) are described in more detail in the following Sections 2.2 and 2.4. Stronger magnetic field of 3T is recommended for ASL imaging, but usable results can also be retrieved at the strength of 1.5T [32]. Another major advantage

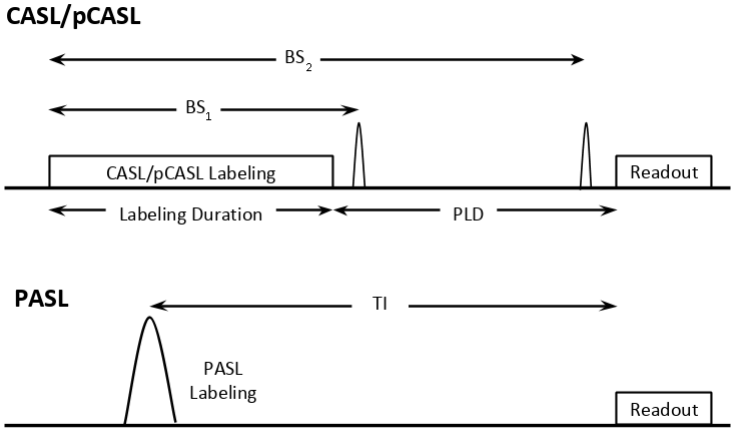

Figure 2.1: CASL and PASL sequences
The diagram depicts the process behind the two main labeling sequences - pulsed labeling and continuous labeling. Courtesy of Yuriko Suzuki and OSIPI TF4.1.
(https://www.osipi.org/task-force-4-1/)

is the usage of phased array coils, which enable parallel imaging [33] and provide with shortened imaging duration.

There is also a solid base in the literature showing that ASL has reached a reasonable reproduciblity in multi-center studies [34], comparable quantitative accuracy with the gold-standard for perfusion image $^{15}O - H_2O$-PET imaging [35], and that ASL has a wide range of clinical applications [36]. All these advancements taken together show that ASL is ready for its translation to clinical practice.

2.2 Labeling sequences

There are two basic labeling strategies commonly used for ASL: pulsed labeling and pseudo-continuous labeling. The diagrams visualizing the process of pulsed and pseudo-continuous labeling are shown in the Figure 2.1.

Pulsed arterial spin labeling (PASL) technique consists of a single RF impulse that inverts magnetization in a large slab (15-20 cm) of tissue [37]. The inverted slab includes arteries, therefore the blood is also inverted and then flows to the region of interest. A small gap between the labeling slab and the imaging volume should be present to exclude the unwanted magnetization of the static tissue. For the PASL techniques, the usage of adiabatic inversion pulses is the recommended to suppress the influence of B_1 inhomogeneities that change the RF pulse's efficiency. The significant disadvantage of PASL is a relatively small (compared with CASL or pCASL) temporal width of the bolus [38]. Moreover, the labeled blood from the distal side of the inversed slab needs longer time to reach the imaging plane, during which the labeling efficiency decreases. This together leads to a notably lower SNR of PASL compared with CASL or pCASL.

Pseudo-continuous labeling (pCASL) is implemented by a long train of many RF pulses on a thin section that produces the longitudinal magnetization inversion of the proximal blood flow to the imaging region [39], [40]. The method originally started as continuous labeling (CASL) approach with a continuous RF pulse [30], however, pCASL has become a preferable method nowadays due to lower unwanted magnetization-transfer effects. Furthermore, a continuous application of RF power is needed for CASL, which leads to a higher specific absorption rate than that of a long train of RF pulses in the pCASL sequence. Unlike in PASL, the pCASL labeling is not instantaneous but takes 1-2 seconds. A similar post-labeling delay (PLD) as for PASL is then applied, making the TR of a single pCASL measurement longer than for the PASL measurement. The choice of optimal PLD is strongly dependent on the relaxation time (T1) of the water molecules in the blood and the time needed for a bolus of blood to arrive at the ROI. The longer is PLD, the more labeled water molecules will arrive at the target tissue, which generates a valuable perfusion signal. With too short PLD, the label does not reach the tissue and stays in the vessels producing macrovascular artifacts [41]. On the contrary, too long PLD leads to the reduction of perfusion signal at the time of imaging. Furthermore, long labeling duration and PLD lead to a longer overall TR and thus a smaller number of averages obtained in the limited acquisition time. Therefore, the optimal PLD is chosen in the interval from 1500 ms (in children) to 2000 ms (in neonates and older people) [32].

2.3 Signal readout

Since magnetic labeling and signal readout are separate processes, multiple combinations of the labeling and readout techniques are possible in ASL. There is only a limited time for the acquisition as the label first needs to arrive to the tissue while quickly relaxing, giving only a short time window for acquisition of signal with reasonable amplitude. Given this condition, fast readout sequences are needed to capture the relevant signal in the brain. There are multiple fast acquisition methods suitable for this task - 2D EPI, 2D multiband (MB), 3D GraSE, or 3D stack-of-spirals. The scope of this work covers data acquired with 2D EPI and 3D GraSE, though similar principles would also apply to 2D MB and 3D stack-of-spirals.

2D Echo-Planar Imaging (EPI) is an MRI signal acquisition technique that enables a fast readout of 2D planes (typically around 20-100ms per slice) [42] [43]. For this, a series of frequency-encoding gradients and a series of intermediary phase-encoding gradients are applied to read the signal from the whole k-space of a single slice in a line-by-line manner after a single excitation pulse. For the means of ASL imaging, multiple 2D slices are obtained that compose a 3D image. The consequences of 2D EPI acquisition for ASL imaging is that slices are acquired in a serial manner and each slice is effectively acquired at a different value of post-labeling delay.

3D Gradient Spin Echo (GraSE) is a hybrid technique that is based on the combination of spin-echo and gradient-echo sequences. GraSE applies an initial 90° RF pulse that is then followed by a series of several 180° refocusing pulses creating several spin echos [44].

The spin-echo technique is further combined with the gradient echo method that creates a series of gradient echoes between each two spin-echoes by rapid switching of the direction of gradients in the readout-direction. The negative frequency-encoding gradient is used to induce transverse dephasing of the spinning protons, and then it is reversed to be used for the readout as spins refocus. This combination enables a rapid signal acquisition of a 3D volume with only one excitation pulse. The technique was at first underestimated due to lower SNR compared to 2D EPI but is getting more recognized nowadays, as stronger magnetic fields (e.g., 3 tesla) are available. Furthermore, 3D GraSE is finding its applicability specifically in the ASL MRI image acquisition due to its rapid readout, whole-brain coverage, and higher SNR. Moreover, a single excitation for the whole volume has two advantages for ASL. The whole volume is acquired with the same PLD, and also with the same amount of background-suppression [45]. It is thus easier to optimize the readout both in terms of perfect static tissue suppression and homogeneous PLD in the whole volume.

To summarize, a 2D EPI image is generated with multiple excitation pulses to acquire the image in a slice-wise manner. In contrast, 3D image acquisition relies on a single excitation pulse. Thus, in the case of 2D EPI, the image slices are effectively acquired at different time points after the labeling; for 3D GraSE, the whole image is excited using a single pulse and thus the image intensities reflect the state of label arrival at a single moment in time. In the context of this work, this difference is worth a special notice because it impacts the amount of background suppression and thus also the signal correction in the control scans.

2.4 Background suppression

Considering that ASL signal intensity is only a few percent of the control image intensity, noise in the static tissue plays a major role in the imaging quality. To improve SNR in ASL MRI, it is essential to suppress the signal from the static tissue and thus reduce the related source of noise caused by thermal and nonthermal fluctuations (e.g., spontaneous neuronal activity, heartbeat, and breathing) [46]. A combination of additional spatially-selective saturation pulses in the imaging volume followed by several spatially non-selective inversion pulses is applied to the tissue to suppress the static tissue signal. An even number of inversion pulses is applied to ensure that the labeled blood is only minimally affected [47]. By use of several inversion pulses and fine-tuned timing of their application at specific background suppression times, an effective suppression of signal with several T1-times can be achieved.

The majority of BS sequences starts with a spatially selective 90° saturation of the imaging field of view, which is followed by multiple spatially non-selective inversion pulses (affecting both the labeling and the imaging areas) as shown in Figure 2.2. There are several inversion pulse designs - the hyperbolic secant, hyperbolic tangent, WURST pulse (wideband, uniform rate, smooth truncation), and broadband inversion pulse. The highest efficiency is typically achieved for the pulses that are barely adiabatic because if it sweeps for a too long time, it introduces T2 decay during the inversion, while if the sweeping is

too fast, the adiabatic condition is not met. The inversion pulses are timed so that at the moment of acquisition, the longitudinal magnetization of selected tissues (based on their T1-time and background suppression timing) is equal or close to zero (example for 2D EPI sequence shown in the Figure 2.2).

The signal changes in the static tissue follow the spin-lattice relaxation (chracterized by T1 time). After the initial 90° pulse, the net longitudinal magnetization is equal to zero and grows back following the spin-lattice relaxation equation (2.1). The 180° background suppression pulses cause further inversion of the longitudinal magnetization vector and the signal changes can be modeled with the Equation (2.2).

$$M_t = M_0(1 - e^{-t/T1}), t \in [0, t_1) \tag{2.1}$$

$$M_t = M_{t_N}(1 - 2e^{-t/T1}), t \geq t_N \tag{2.2}$$

M_t = magnetization at time t
M_0 = magnetization just before the 90° pulse
$T1$ = relaxation time of the tissue.
t_N = time of the N-th 180° inversion pulse

The inversion can be also described by the Equation (2.3)

$$M_{t_i} = -\alpha_{BS} \cdot M_{t_{i-\epsilon}} \tag{2.3}$$

α_{BS} = inversion pulse efficiency
ϵ = inversion duration

For simplicity, the inversion is assumed to be instantaneous ($\epsilon = 0$).

The inversion pulses do not cause a perfect inversion while affecting the signal inversion in the static tissue and causing attenuation of ASL signal through multiple background suppression pulses as well. Typical efficiency of the inversion pulse α_{BS} is around 95% for each pulse [32]. Noteworthy, the longitudinal magnetization of the selected tissue(s) is perfectly nulled out only at a certain moment in time, after which it continues to grow back to the equilibrium with T1-relaxation. This is why the 3D GraSE readout sequence, with a single excitation, can provide a perfect suppression in the whole-brain. While the 2D EPI readout with sequential signal excitation for each slice has a different level of background suppression in each slice, see Section 2.2 [48].

2.5 Partial volume correction

The resolution of ASL imaging is lower compared with most other MRI imaging methods and lower to that of most cortical structure. This leads to a so-called partial volume effect (PVE). PVE is characterized by the fact that most individual voxels typically contain a

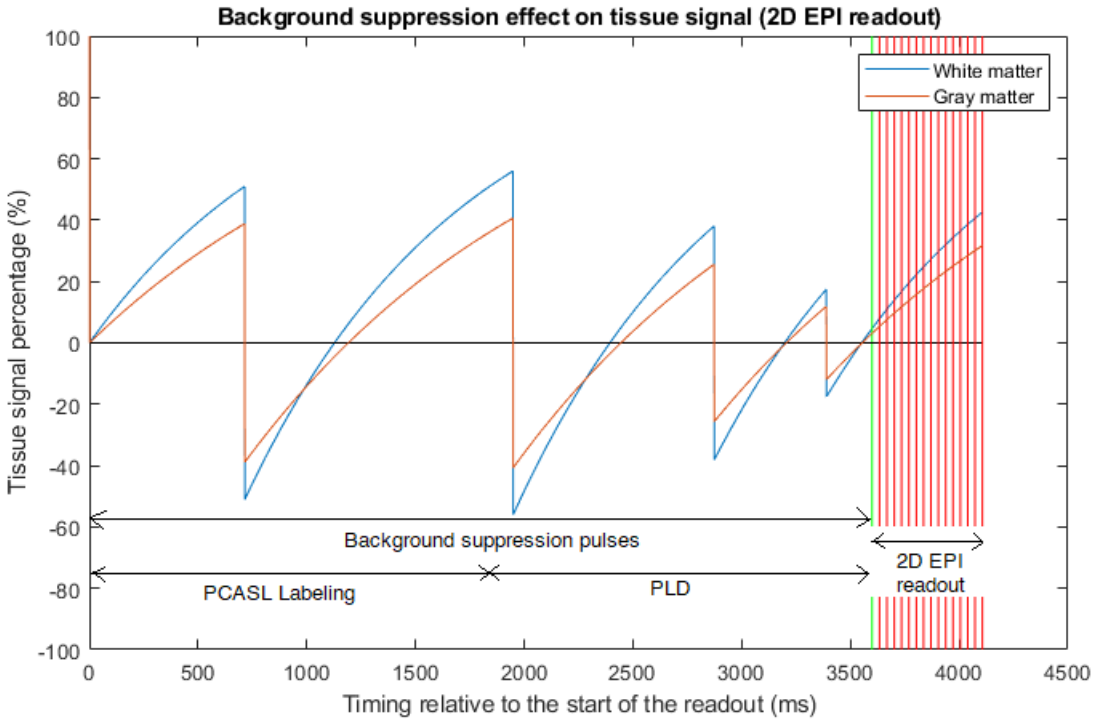

Figure 2.2: The model of background suppression sequence in 2D EPI
The plot shows the difference between the background suppression efficiency for white (shown in blue) and gray (shown in orange) matter in the context of ASL imaging with pCASL 2D EPI sequence. The green vertical line indicates the start of the readout, with the following red lines indicating the scanning times of the succeeding slices.

mixture of gray matter (GM), white matter (WM), and cerebrospinal fluid (CSF) that have different magnetization properties (Figure 2.2). CBF in GM is around 2-3 times higher than in WM and no CBF is expected in CSF. This makes the voxel-wise CBF strongly dependent on the tissue composition [49]. Many clinical applications of ASL imaging focus on measuring CBF in gray matter. Since gray matter can be as thin as 2 mm in normal adults, PVE can lead to serious errors in the estimation of GM CBF when measured with ASL [50].

Multiple methods dealing with PVEs in CBF quantification have been proposed [51]. The most common method is based on evaluating CBF only in voxels that have a GM content higher than a given threshold (usually a threshold of 0.8 or 0.7 are used). GM thresholding can, however, lead to uneven distribution of evaluated voxels in space, and does not remove the effect of CBF underestimation completely. An alternative is to use partial volume correction (PVC) through linear regression. This PVC method assumes constant true tissue perfusion CBF_{GM} and CBF_{WM} in a local neighborhood, and with the knowledge of the tissue distribution in each voxel, it can obtain the true perfusion values through solving a system of linear equations [50].

2.6 CBF Quantification

The most important parameter that is obtained from ASL MRI data through quantification is CBF. The CBF quantification is based on further assumptions that might differ depending on the choice of the labeling or readout sequence [32] [52]. The CBF quantification follows following assumptions:

1. The labeled bolus has to arrive completely to the target tissue. For pCASL, this is the case when post labeling delay is longer than the arterial transit time; for PASL, the difference between the inversion time and bolus duration (analogous to post labeling delay) has to be larger than the arterial transit time;

2. No outflow of labeled blood water, since the tissue has a large water pool and there is a fast exchange of particles between tissue and blood;

3. The relaxation of the labeled particles depends on blood T1.

With these assumptions, the CBF for pCASL is calculated as

$$CBF = \frac{6000 \cdot \lambda \cdot \Delta M \cdot e^{\frac{PLD}{T_{1b}}}}{2 \cdot \alpha \cdot T_{1b} \cdot M_{0t} \cdot (1 - e^{\frac{-\tau}{T_{1b}}})} [ml/100g/min]$$

λ = brain-blood partition coefficient in mL/g
ΔM = difference in longitudinal magnetization
T_{1b} = T1 relaxation time of blood in ms
α = labeling efficiency
M_{0t} = equilibrium magnetization of tissue
τ = label duration
PLD = post-labeling delay

Note that for 2D imaging, the effective PLD value has to be adjusted by adding the slice-timing value per every slice. A separately acquired M0 image is used to obtain the values of M_{0t} and to also indirectly reduce the effect of coil inhomogeneity. The blood-brain partition coefficient λ is used to convert the tissue magnetization M_{0t} to that of blood M_{0b}. Ideally, λ should be adjusted voxel-wise to tissue type, since water density varies across brain tissues. The M0-scan is usually spatially smoothed with subsequent division by the brain average brain-blood water partition coefficient λ [23].

Even though this model is simplified, it is still recommended for its robustness and lower requirements on data and parameters (e.g., there is no need to calculate arterial transit time) [53].

2.7 Toolboxes for ASL MRI Processing

The current trend is to use a robust pipeline for processing MRI data instead of writing ad-hoc in-house script for each clinical study. There are multiple pipelines available for ASL image processing, as for example ASL-MRICloud [54], ENABLE [55], or Quantiphyse [56]. However, the focus of this work is on the ExplroeASL - another up-to-date toolbox that comprises all functionality needed for ASL image processing.

Most of the work presented in the thesis was implemented in the ExploreASL pipeline for processing ASL MRI data [31], which is available on the website www.ExploreASL.org. It is developed in MATLAB (Mathworks, Nattick, US) and uses Statistical Parametric Mapping (SPM) [57]. This toolbox provides multiple useful features, e.g., flexible data import and management (anonymization, compression of image files, and optional defacing), modular design (which allows easier iteration through multiple subjects' scans), specifically optimized image processing procedures, extensive quality control, etc. The pipeline consists of 4 modules: import, structural, ASL, and population.

2.8 BS correction for M0 calculation - current developments

While several approaches for estimation of blood M0 are available [32], [58], only minimal attention was dedicated to different processing strategies for M0 images. One of the studies that focuses on the processing of M0 images is by Pinto et al. [23], which demonstrates the importance of the M0 estimation as one of the two most important factors in CBF quantification and provides an extensive overview of various M0 calibration post-processing approaches. This study covers the comparison of three M_{0t} estimation methods: long TR calibration scan, control image averaging, and control saturation recovery. The results emphasize the importance of the incomplete T1 magnetization correction and correction for RF field inhomogeneities. For the course of the given work, it is important to notice that the T1 correction plays a major goal in the method sensitivity.

This and other research works have been focusing on M0 quantification from a dedicated M0 scan. Nonetheless, the inconspicuous challenge that appears in practice is that M0 scans can be lost during data acquisition or data transferring, or simply not acquired at all. This creates an obstacle for clinical studies that aim for absolute CBF quantification without having M0 images readily available, while having obtained control images with BS. This is especially problematic in multi-center datasets that use different sequences and scanners where relative differences in CBF values between datasets can occur if use of an M0 scan is omitted in the quantification.

Correction of signal from control images with BS is done only rarely and not in the context of CBF quantification but rather that of artifact correction. An example is the study by Suzuki et al. [59], which focuses on the motion correction in MB acquisition with BS. Unlike in standard 2D images with smooth increase of slice-time and BS-level over slices, in 2D MB, the slice time and BS efficiencies change sharply between slices

from two different groups. This is an important issue in combination with motion as even with correct realignment, these sharp contrast transitions are not removed in motion correction resulting in motion artifacts. Modeling the BS effect is used to homogenize the signal in control images over different slices to reduce the contrast changes between slices. Subsequently, the amount of artifacts is reduced after motion correction compared with the non-BS corrected approach.

In conclusion, the challenge of blood M0 estimation from the control scans with background suppression has not been addressed before, even though publications exist addressing the relevant individual components of this issue. In this work, we present a solution to this challenge and validate its accuracy and reproducibility in examples with both 2D and 3D readouts.

Chapter 3

Methods

The main goals of the thesis were to assess and quantitatively compare different approaches of M0 image estimation from control scans acquired with BS to derive the optimal approach that would result in an accurate CBF quantification. All M0 images were estimated from control scans with BS with the correction for the effects of BS. The main challenge laid in the fact that different tissue types (WM, GM, and CSF) are present in each voxel and that these tissues have different T1 values, thus being differently affected by the BS. This issue was addressed with partial volume (PV) effect correction to derive the accurate tissue-dependent signal and to run dedicated tissue-specific BS correction in the separate voxels according to their PV content. The central hypothesis of this work was that by correcting for the BS signal changes and the PV effect, M0 scans could be estimated from control images with BS leading to CBF quantification with sufficient accuracy and repeatability and comparable to the CBF derived from real M0 scans.

The course of the following work comprised the experiments to test these hypotheses. In order to get better acquainted with the properties of the input data, an initial analysis was done that included the comparison of signal intensities in the regions of interest and given different readout sequences and labeling schemes acquired in healthy volunteers. The dataset consisted of both 2D EPI and 3D GraSE readout scans that included labeled scans with BS, control scans with BS, and reference M0 scans (Table 3.1). Afterwards, a series of experiments was conducted to estimate M0 image based on the BS correction in the control scans and to assess the accuracy of the estimation. This part consisted of testing two different approaches:

1. Applying BS correction assuming a single tissue type with a single T1 value over the whole brain,
2. Assuming a mixture of tissue in every voxel and applying BS correction with prior PV correction.

The accuracy of the methods was evaluated using reference M0 scans. Additionally, the stability of the methods was assessed in the within-subject comparisons to display the results reproducibility. Consequently, the M0 estimation methods were incorporated into the

ExploreASL pipeline, and the accuracy and the stability of resulting CBF were calculated. Finally, the results were interpreted, and the optimal approach was defined that answered the initial hypothesis and laid the ground for future work.

3.1 Subject information

The image acquisition was conducted following the Declaration of Helsinki guidelines and under a waiver of institutional review board approval by the Medical Research Ethics Committees United (Nieuwegein, the Netherlands) [60]. All participants provided written informed consent and received remuneration for their participation. The participants were used to stay still during the MR scanning and were instructed to abstain from caffeine and smoking during the whole experiment. More detailed information about the subjects is provided in Table 3.1. Evidently, the data were acquired in healthy volunteers, with some of them being of older age and having representatives of both sexes.

Subject Label	Age	Sex	Weight
V04S02	46	M	95
V05S01	63	M	74
V06S02	67	F	60
V08S02	74	M	71
V09S01	80	M	78

Table 3.1: Subjects information

3.2 Data acquisition

The data were acquired on the Ingenia scanner at 3T magnetic field strength at Philips Healthcare headquarters in Best, the Netherlands [60]. For brain image acquisition, the 15-channel head coil was used with the scanner software version R5.4.

The experimental sessions were conducted in the following order:

1. 3D T1-weighted scan, which was used in the processing of the ASL image as the anatomical reference.

2. Two identical pCASL scans with 3D GraSE readout sequence with the standard PLD of 1800 ms. Every scan included 2 M0 images, 7 control scans with BS, and 7 labeled scans with BS.

3. Two identical pCASL scans with 2D EPI readout sequence with the standard PLD of 1800 ms. Every scan included 2 M0 images, 29 control scans with BS, and 29 labeled scans with BS.

To simplify the further description of the acquired data, every given scan was given a separate name. More info on the the pCASL scans and their names is listed in the Table 3.2. Both for 3D GraSE and 2D EPI, 4 BS pulses were applied with following timings: 716 ms, 1949 ms, 2875 ms, 3391 ms.

Readout	TR (s)	TE (s)	PLD (s)	Labeling duration (s)	Repeats	Voxel size (mm)	Matrix	Names
3D GraSE	4.2	0.012	1.8	1.8	7	3.75 x 3.75 x 6	64 x 64 x 14	3D-1-1800, 3D-2-1800
2D EPI	4.2	0.0112	1.8	1.8	29	3.75 x 3.75 x 6	64 x 64 x 16	2D-1-1800, 2D-2-1800

Table 3.2: Scan info and names

Image acquisition was conducted in agreement with the consensus recommendation on ASL implementation [32]. The labeling plane was positioned 9 cm below the bicommissural line. To verify the position of the labeling plane, a phase-contrast angiography survey scan was conducted. In some cases, the distance was adapted to avoid the overlap between the labeling slab and carotid siphon to provide with homogeneous labeling and to avoid the overlap between labeling and imaging planes.

The examples of the M0 image, control scan with BS, and the resulting CBF image are shown in Figure 3.1.

3.3 Data pre-processing

Throughout the work on the thesis, the data were processed using the ExploreASL pipeline [31]. Firstly, the T1-weighted images were spatially normalized and segmented into WM, GM, CSF using CAT12 toolbox [61]. The generated spatial maps had values ranging between 0 and 1 and denoted a relative tissue content in each voxel. Then, ASL, T1-weighted, and M0 images were co-registered. Afterwards, the GM and WM maps were transformed to the ASL space and subsampled to the same resolution.

To perform M0 image estimation, the pipeline was paused before M0 processing. To calculate the resulting CBF, the ASL module was altered to include the implemented M0 estimation methods. Therefore, all the data preprocessing steps, processing of M0 image (e.g., masking and smoothing), and CBF quantification steps were maintained the same for real M0 image and estimated M0 image.

The GM and WM maps were then used to define masks of the ROIs. These regions include deep WM, GM, and CSF. Since these maps have the same resolution as ASL image, a single voxel can contain a mixture of GM and WM (with different relative content), the thresholding was defined to derive masks of voxels with predominately GM or WM content.

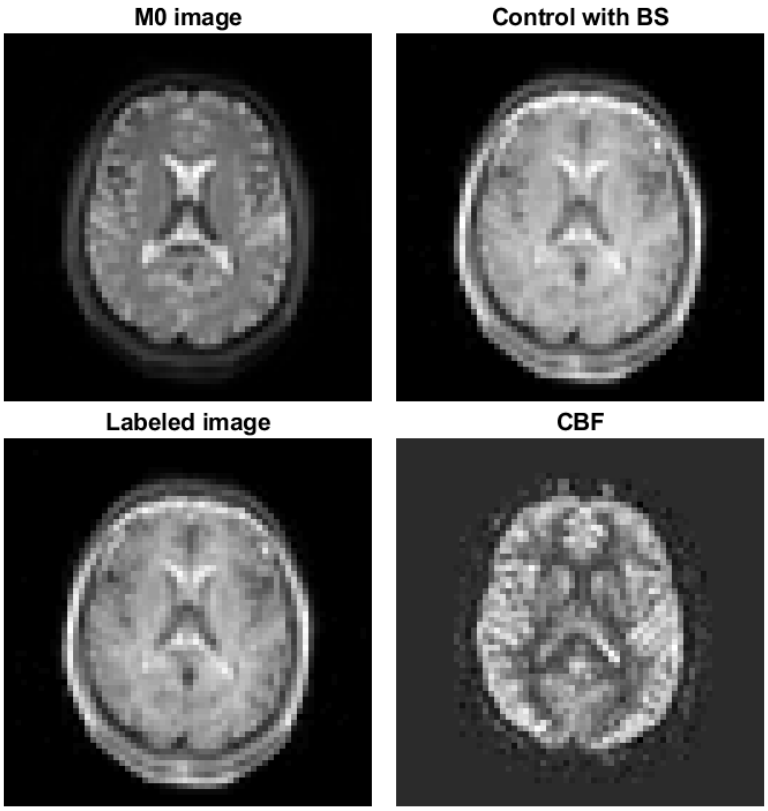

Figure 3.1: M0 image, control scan with BS, labeled scan with BS, and resulting CBF CBF image was calculated with ExploreASL (Subject: V04S02, sequence: 3D-1-1800).

For a general overview of the WM, GM, and CSF, the threshold value of 0.5 was used. These masks are contaminated with the presence of other tissue, but cover a larger number of voxels, which is beneficial to study a common trend in the tissue. The examples of these thresholded masks for WM and GM are visualized in Figure 3.2. These masks are references as *GM-mask-50*, *WM-mask-50*, *CSF-mask-50* in the further text.

To restrict the experiments on the deep WM, two different deep WM masks were estimated by thresholding the PV map with furhter erosion [62]. First, the PV in the WM map was thresholded (dWM-mask-50-2: threshold = 50%; dWM-mask-80-1: threshold = 80%). Consequently, the Euclidean distance from the mask edge in 3D was calculated using the Borgefors Chamfers equation. The outer layer of voxels was removed (dWM-mask-50-2: distance = 2; dWM-mask-80-1: distance = 1) and only the inside of the mask was kept. As a result, the first mask (dWM-mask-50-2, Figure 3.3) had less GM contamination, but the second mask (dWM-mask-80-1, Figure 3.4) had more voxels.

To restrict the experiments on GM, we used a GM mask - GM-mask-65 (Figure 3.5). Unlike the experiments with the WM mask, thinning was not included because the GM is a few voxels thin in general and thinning would thus not make sense. To obtain the GM mask, the GM map was thresholded with a value of 65%.

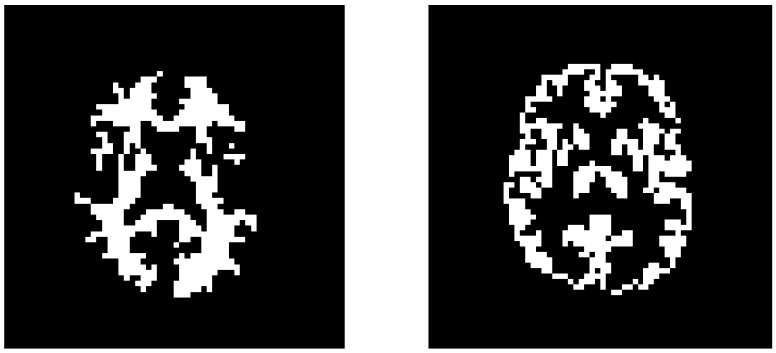

Figure 3.2: Thresholded WM and GM maps
The white matter map (WM-mask-50) is on the left, the gray matter map (GM-mask-50) - on the right.

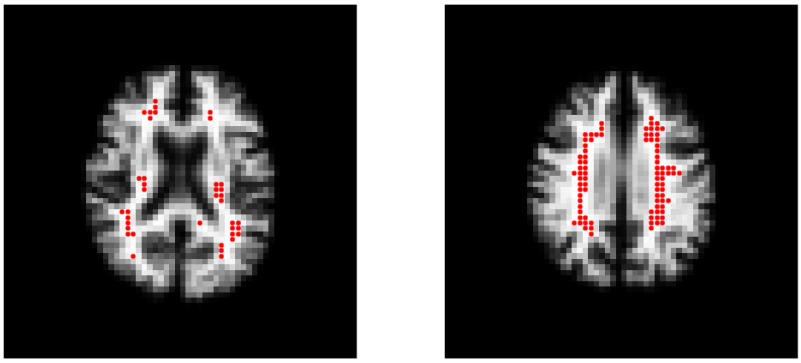

Figure 3.3: Visualization of dWM-mask-50-2
The mask is shown in red dots over a slice of WM map visualized in grayscale. Sequence: 3D-1-1800, slices 7 and 9.

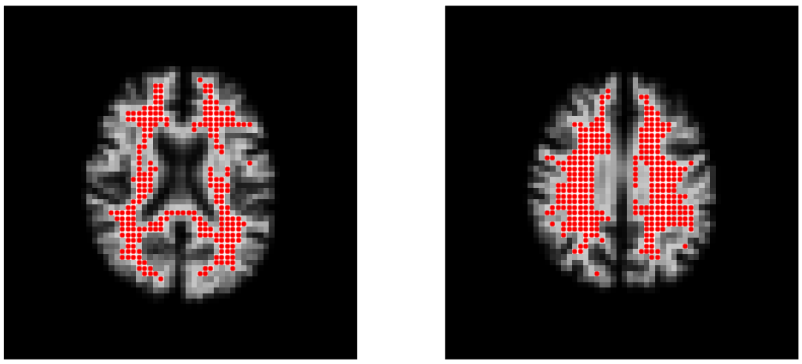

Figure 3.4: Visualization of dWM-mask-80-1
The mask is shown in red dots over the slice of WM map visualized in grayscale. Sequence: 3D-1-1800, slices 7 and 9.

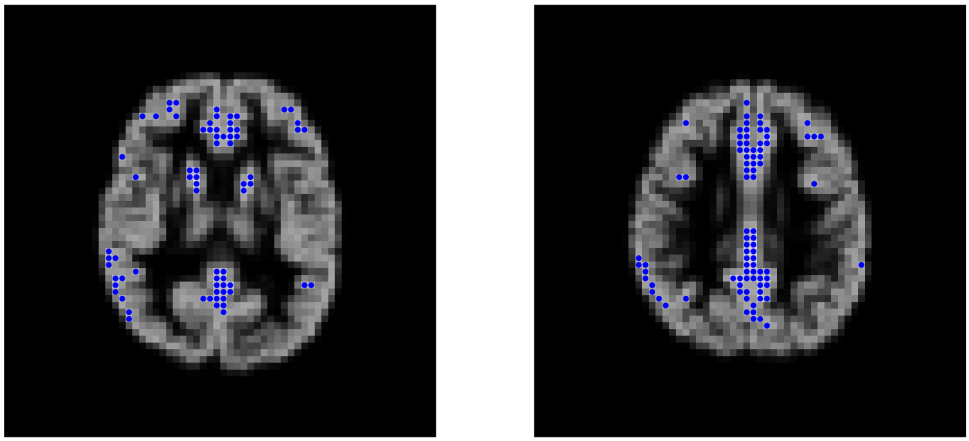

Figure 3.5: Visualization of GM-mask-65
The mask is shown in blue dots over the slices of gray matter spatial map visualized in grayscale. Experiment: 3D-1-1800, subject: V04S02, slices 7 and 9.

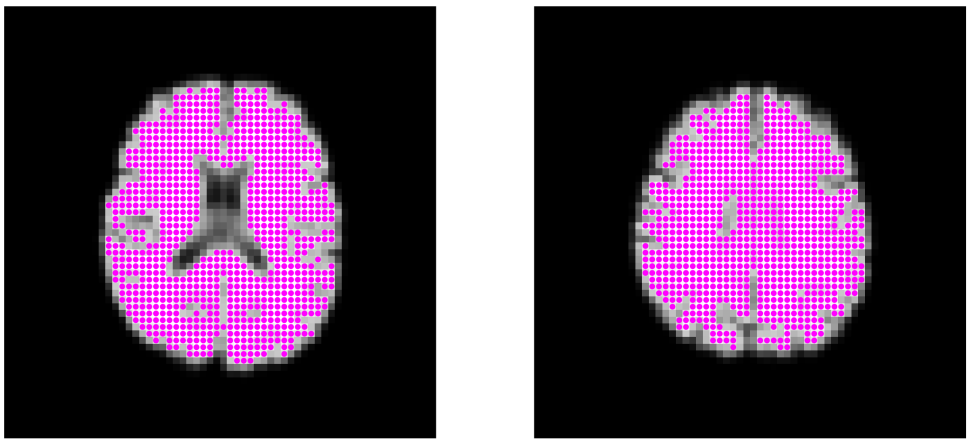

Figure 3.6: Visualization of WMGM-mask-80
The mask is shown in magenta dots over the slices of GM and WM maps visualized in grayscale. Sequence: 3D-1-1800, slices 7 and 9.

Finally, the whole brain mask was calculated (WMGM-mask-80) by calculating the sum of WM and GM maps and thresholding it at 80% (Figure 3.6).

The deep WM (dWM-mask-50-2, dWM-mask-80-1) and GM (GM-mask-65) masks were used to evaluate M0 estimation with tissue differentiation, whereas whole brain mask (WMGM-mask-80) was used to evaluate M0 estimation without tissue differentiation.

3.4 Description of the conducted experiments

In order to test the hypothesis of accurate M0 image estimation from the control scans, the following experiments were covered in the course of this work:

1. **Initial analysis** of the acquired data to study the differences in signal distribution in true M0 images among subjects and spatial location, depending on the readout sequence.

2. **M0 estimation using BS correction** from the control scans, where the correction was done with a single T1-time value in all voxels assuming a single tissue type.

3. **Use of PV effect correction and mixed-tissue model** for the M0 image estimation. The signal contribution for different tissue types was separated using PV correction. BS correction was then done separately for each tissue type using the respective T1-time to obtain the estimated M0 in a mixed-tissue model.

4. **Comparing resulting CBF** between quantification using the estimated and reference M0 scans.

3.4.1 Error calculation

To quantitatively assess the difference between the estimated M0 scan and the reference scan, to compare the resulting CBF maps derived using the estimated M0 scan, and to test the reproducibility of the M0 estimation, we defined the following parameters.

The mean relative error (MRE) was defined as

$$MRE_{slice} = \frac{\sum_{x \in mask} \frac{Im_{est}(x) - Im_{ref}(x)}{Im_{ref}(x)}}{N_{slice}} \tag{3.1}$$

where *slice* refers to the slice of the given *mask*, $Im_{est}(x)$ indicates the estimated value in voxel x, Im_{ref} is the reference value, and N_{slice} is a number of voxels in the given slice. In the context of the thesis, the MRE was calculated for images Im being M0 or CBF.

To estimate the within-subject inter-session repeatability, a within-subject root-mean-square error (WS RMSE) was used:

$$WS\ RMSE_{slice} = \sqrt{\frac{\sum_{x \in mask} \left(\frac{Im^A_{est}(x) - Im^A_{ref}(x)}{Im^A_{ref}(x)} - \frac{Im^B_{est}(x) - Im^B_{ref}(x)}{Im^B_{ref}(x)} \right)^2}{N_{slice}}} \tag{3.2}$$

where *slice* refers to the slice of the given mask, Im^A_{est} and Im^B_{est} refers to the estimated value in the first and the second dataset, respectively (e.g., 2D-1-1800 and 2D-2-1800), Im_{ref} is the reference value in the given dataset, and N_{slice} is a number of voxels in the given slice.

To assess the MRE variation across slices, a standard deviation in across slices was calculated for subject-averaged MRE std^{MRE}_{slices}.

To assess how MRE variability in the population, a standard deviation across subjects was calculated on slice-averaged MRE $std^{MRE}_{subjects}$.

In both cases, the most superior and inferior slices were excluded due to a minimal number of voxels on the masks, leaving slices 3-12 for 2D EPI, and 2-12 for 3D GraSE.

3.4.2 Initial analysis

Signal distribution in 2D EPI and 3D GraSE. To better understand the input data, the mean signal intensities in control scans and M0 images were calculated for each slice. This is important to show the signal distribution in M0 images across slices, the level of BS in the control images, and the level of BS in the WM and GM using the masks WM-mask-50 and GM-mask-50, respectively.

Signals distribution in M0 images. Here, the signal intensities in M0 images in subjects in WM, GM, and CSF were calculated using WM-mask-50, GM-mask-50, and CSF-mask-50.

3.4.3 M0 estimation using BS correction

These experiments focused on the signal corrections in the control scans. The known BS timings were used to estimate the factor of BS correction in each slice based on the T1 value. The correction also accounted for 95% efficiency of the BS inversion pulse (Section 2.4). Afterwards, the signal in the controls was divided by this factor to compensate for BS and to estimate the M0 image without BS. Due to lower resolution of ASL, most voxels contain a mixture of tissues with different T1 values. Therefore, we have tested different T1 values relevant to a selected ROI to find values that provide an optimal correction for BS. The results were compared with the reference M0 scan, and their accuracy and stability were assessed.

The estimated M0 image was calculated with the given equation

$$M_0^{est} = \frac{M_{control}}{BS_{coef}}, \tag{3.3}$$

where $M_{control}$ indicates the signal intensity in the control scan with the BS correction and BS_{coef} is the background suppression coefficient, which corrects the control image according to the timings of the BS pulses. Next, the accuracy of the M0-estimation was assessed with MRE calculation in estimated M0, M_0^{est}, and true M0. The number of voxels in the mask and the amount of GM and WM content was calculated for each slice to investigate the effect of noise and the effect of mixed tissue content on estimation assuming a single-tissue model. Next, the stability of M0 estimation was assessed using the WS RMSE in M0 scans.

To restrict the experiments on the deep WM, dWM-mask-50-2 and dWM-mask-80-1 were used to mask the images (Section 3.3). For the experiments on the deep WM masks,

a range of T1 values from 750 up to 1200 ms was tested. Experiments continued with the calculations in GM using GM-mask-65. T1 values for the BS correction in GM were chosen in the range from 1050 ms to 1500 ms. Finally, the experiments in the whole brain were conducted using WMGM-mask-80 with T1 values in the range from 1000 ms up to 1400 ms (values in between those suitable for deep WM and GM, since the whole brain mask consists of both). In all the ranges, the increment of 50 ms was used.

3.4.4 Experiments with partial volume correction

The PVC (mixed-tissue) approach was applied to the control scans to compensate the BS correction difference in both WM and GM, which have different T1 values. The correction was done using prior GM- and WM-partial volume maps according to the regression algorithm correcting for partial volume effects in ASL MRI described by Asllani et al. [50]. Generally, the WM and GM tissue contribution to the signal was estimated using the following equation

$$M_{control}(x) = P_{WM}(x) \cdot M_{control,WM}(x) + P_{GM}(x) \cdot M_{control,GM}(x), \tag{3.4}$$

where $M_{control}(x)$ denotes signal intensity in a voxel of the control scan, $P_{GM}(x)$ and $P_{WM}(x)$ denote tissue partial volume in GM and WM, respectively, in a voxel x and $M_{control}(x)$ denotes tissue longitudinal magnetization contribution to the signal intensity in a given voxel. In each voxel x, a system of linear equations was created from equation 3.4 by assuming that $M_{control,WM}(y)$ and $M_{control,GM}(y)$ are constant in voxels y in the neighborhood of x, this system was then solved in the least squares sense. Unlike in the original work by Asllani, a Gaussian kernel with FWHM $5 \times 5 \times 5$ voxels was used instead of a flat kernel. Moreover, the calculation was restricted to WMGM-mask-80 to accommodate the fact that the signal contribution of CSF to M0 is, contrary to CBF, nonzero.

After the $M_{control,GM}$ and $M_{control,WM}$ were estimated, they were further used to separately correct the background-suppressed signal in tissue to achieve estimation of the M0 image using the following equation:

$$M_0^{est}(x) = (P_{WM}(x) \cdot \frac{M_{control,WM}(x)}{BS_{coef,WM}}) + (P_{GM}(x) \cdot \frac{M_{control,GM}(x)}{BS_{coef,GM}}), \tag{3.5}$$

where $BS_{coef,GM}$ and $BS_{coef,WM}$ denote the BS coefficient (Eq. 3.3) using the WM and GM specific T1-time values, respectively. This approach aimed at decreasing the error caused by differing T1 values. The T1 values used for BS correction in GM and WM were derived from the experiments on M0 estimation describes in section 3.4.3: for GM, T1 was chosen based on the experiments in GM-mask-65, for WM - from experiments in dWM-mask-50-2 and dWM-mask-80-1.

3.4.5 Comparing resulting CBF

The most common goal of ASL imaging is quantification of CBF using the calibration M0-scan. To test the validity of M0 image estimation in practice, the resulting CBF values were

compared for different approaches of M0-scan estimation from control images as described in previous parts.

Two main M0-estimation approaches were compared in this part: the application of BS correction using a single T1 value for the whole brain and the application of BS correction using PV-corrected tissue-specific T1 values. Both methods were incorporated within the ASL module of the ExploreASL pipeline, and the estimated M0 image was then conventionally processed (with consequent masking and smoothing). The optimal T1 values used for the final assessment were derived from the previous experiments. The T1 value for the whole brain BS correction was derived from the experiments in WMGM-mask-80, whereas the T1 values for the PV correction approaches were derived from the experiments in GM-mask-65, dWM-mask-50-2, and dWM-mask-80-1. Again, the MRE of the resulting CBF values was calculated for the ROI compared to the reference CBF values. Furthermore, the WS RMSE was estimated for the assessment of the reproducibility. To also assess the perseverance of the error in slices and subjects, std^{MRE}_{slices} and $std^{MRE}_{subjects}$ were also calculated.

Chapter 4

Results

This chapter covers the results obtained in the course of the thesis. The results address the main hypothesis and answer the question if it is possible to estimate M0 scan from control images with BS with both sufficient accuracy and reproducibility.

4.1 Initial Analysis

Mean signal distribution. The distribution of mean signal intensities over the slices in control scans with BS acquired with 2D EPI and 3D GraSE readouts are visualized in Figure 4.1.

Figure 4.1 shows that the signal intensity increases almost six fold towards the superior part of the brain in control scans for 2D EPI, while a slight decrease of around 50% between the first and last slice is noticeable in controls for 3D GraSE. On average, GM has a lower signal intensity comparing to WM in control scans, and higher signal intensity in M0 scans.

The comparison of mean signal intensity (MSI) in tissue is shown in Figure 4.2. The signal distribution in M0 images is more stable in tissue across subjects in 2D EPI (std_{WM}^{MSI} - 67.71, std_{GM}^{MSI} - 54.5, std_{CSF}^{MSI} - 174.28) with the highest signal intensity in gray matter and the lowest in CSF. In 3D GraSE, the signal distribution differs more among subjects (std_{WM}^{MSI} - 116.13, std_{GM}^{MSI} - 118.79, std_{CSF}^{MSI} - 135.97).

4.2 Testing T1 values for M0 image estimation

This section of the Results focuses on the results of estimating M0 from the control scans assuming uniform tissue with a single T1 value in the given ROI. The section is further divided per region of interest. Every following subsection describes both the accuracy and reproducibility of the results.

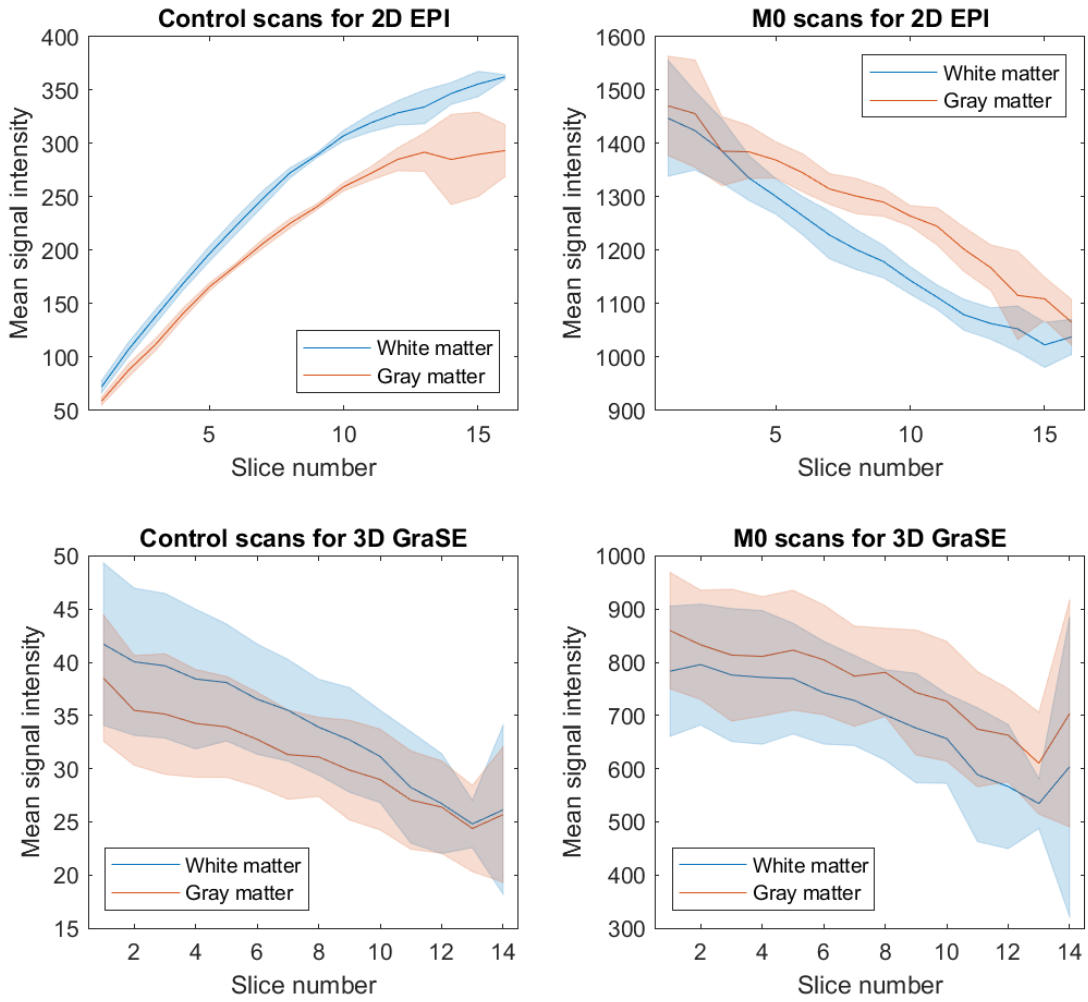

Figure 4.1: Mean signal intensities in controls and M0 scans in 2D EPI and 3D GraSE sequences
Sequence: 2D-1-1800, 3D-1-1800

4.2.1 Deep white matter

The efficiency of M0 image estimation in deep WM using various T1 values in 2D EPI and 2D GraSE data are visualized in the Figures 4.3 and 4.4.

As described in Section 3.3, dWM-mask-50-2 is more conservative with fewer voxels but insignificant content of GM. For dWM-mask-50-2, using lower WM T1-values reduced MRE between reference and estimated M0. Also, due to the smaller number of voxels in the first map, there was a higher variation in MRE among subjects. Both masks depicted that there was a need to decrease the estimated signal intensity in the lower slices. The differences in voxel counts grew towards the higher slices. The results also show that the estimation for both most inferior and superior slices was less reliable and was prone to higher values. For both readouts, the slices with smaller number of active voxels in the

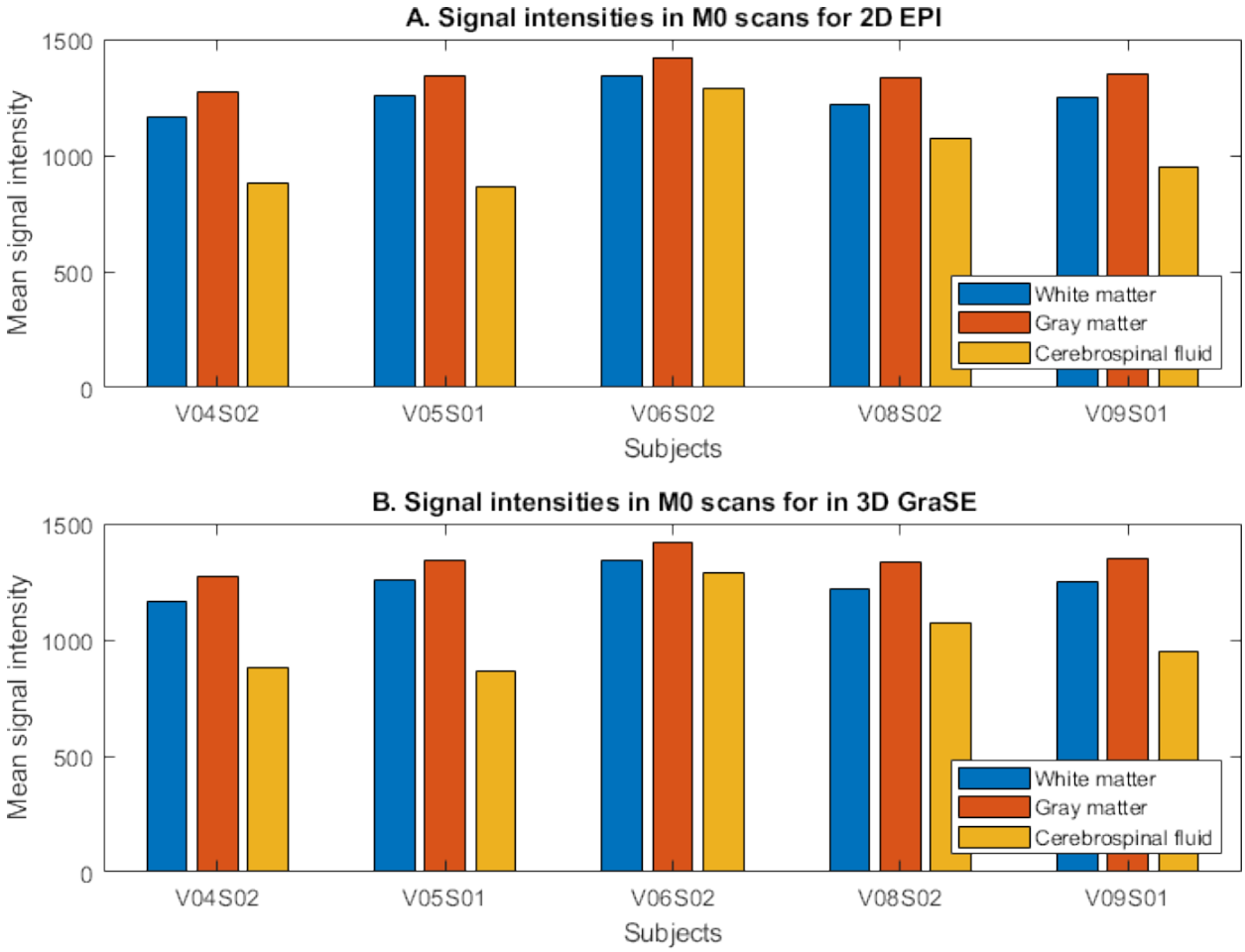

Figure 4.2: Signal intensities in different tissue in M0 image in 2D EPI and 3D GraSE Sequence: 2D-1-1800, 3D-1-1800

maps were prone to higher variation of error.

When comparing the M0 estimation between 2D EPI and 3D GraSE readout sequences, using lower values of T1 in deep WM matter was preferable for 3D GraSE readout. For 2D EPI, the optimal T1 value for deep WM was 1050 ms: for dWM-mask-50-2, its absolute mean relative error was below 5.5% for slices 3-13; for dWM-mask-80-1, its absolute mean relative error was below 2% for slices 3-15. For 3D GraSE, the optimal T1 value for deep WM was 950 ms: for dWM-mask-50-2, its absolute mean relative error was below 5.5% for slices 2-12; for dWM-mask-80-1, it absolute mean relative error was below 5.5% for slices 2-11.

However, the stability of the efficiency across slices was better in 2D EPI compared to 3D GraSE. For 2D EPI, the std^{MRE}_{slices} in central slices was 1.2% for dWM-mask-50-2 and 0.57% for dWM-mask-80-1. For 3D GraSE, the std^{MRE}_{slices} was 3.5% for dWM-mask-50-2, and 4.1% for dWM-mask-80-1.

Within-subject experiments are visualized in the Figure 4.5 for 2D EPI and 3D GraSE

readouts. The stability of the MRE estimation was better in the dWM-mask-50-2 in both readout sequences, which was expected, since this region is more homogeneous. When comparing 2D EPI and 3D GraSE in terms of stability, 2D EPI had lower values of WS RMSE. For both readouts, the variance was higher in the inferior slices, which also have a lower number of active voxels in both masks, leading to lower statistical power. For both readouts, higher values of T1 led to the higher WS variation in MRE. For both of the optimal T1 values (in 2D EPI, T1 = 1050 ms; in 3D GraSE, T1 = 950 ms), the WS RMSE is below 5% for the slices.

4.3 Gray matter

The results estimating the accuracy of signal correction in the gray matter are displayed in the Figures 4.6 and 4.7 for 2D EPI and 3D GraSE readouts respectively. The optimal T1 values for the BS correction in GM mask were higher for 2D EPI than in 3D GraSE. For 2D EPI, the optimal T1 value of GM was 1500 ms: its absolute mean relative error was below 8% for slices 3-12. For 3D GraSE, the optimal value of T1 in GM was 1200 ms, its absolute mean relative error was below 12% for slices 2-12.

As seen on the graphs, the MRE distribution across slices was not homogeneous comparing to the previous experiments in deep WM. For 2D EPI, the std^{MRE}_{slices} was 3.91%; for 3D GraSE, it was 6.34%.

Using such low threshold of the GM mask allowed a comparatively high mean voxel content of WM in the slices, evident from the graph of relative content in GM mask. For the most superior slices, the GM content was lower, which leads to lower statistical power.

When looking at the within-subject stability of the estimations (Figure 4.8), it was evident that the most inferior slices were more unstable in the GM mask with higher variation of voxel counts and content. For the most superior slices, the variation in voxel number was smaller, but the voxel content variation was higher. Compared to deep WM, the WS RMSE was higher, leading to lower stability of the estimation in GM. For both of the optimal T1 values (in 2D EPI, T1 = 1500 ms; in 3D GraSE, T1 = 1200 ms), the WS RMSE was below 10% for slices excluding the most inferior.

4.4 Whole brain experiments

Next, the results visualizing the accuracy of M0 estimation in the WMGM-mask-80 are provided in the Figures 4.9 and 4.10 for 2D EPI and 3D GraSE. The voxel number in this map was large, so the statistical power of estimated MRE was also larger. The lowest MRE corresponded to a T1 value 1200 ms for 2D EPI: its absolute mean relative error was below 5% for slices 3-12. For 3D GraSE, the optimal T1 value for the whole brain was 1050 ms: its absolute mean relative error was below 5% for slices 2-12.

The curves of RME distribution across slices were flat compared do experiments in GM and deep WM. For 2D EPI, the std^{MRE}_{slices} was 1.11%. For 3D GraSE, std^{MRE}_{slices} was 1.27%.

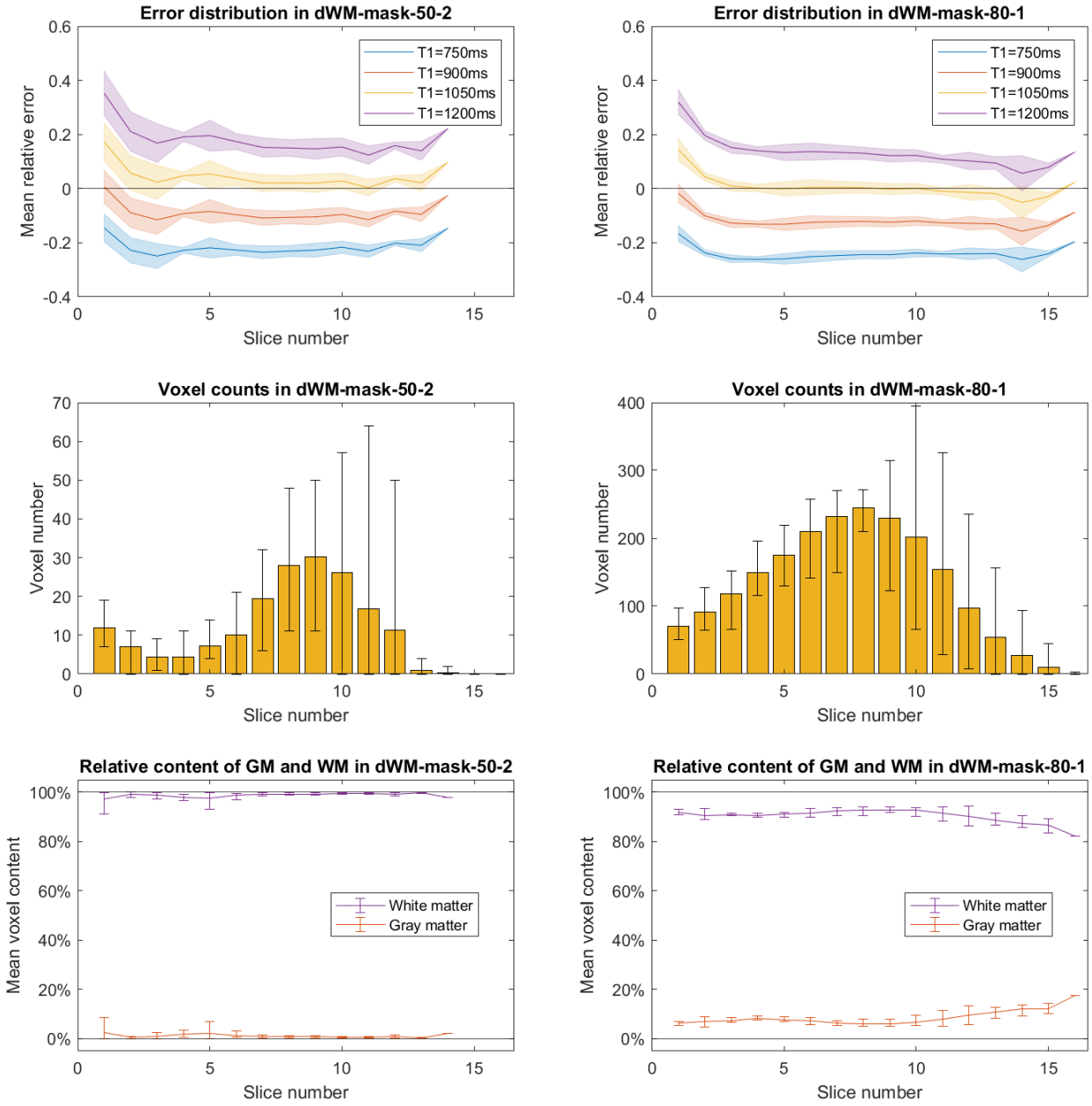

Figure 4.3: Efficiency of M0 estimation in deep WM for different T1 values in 2D EPI in deep white matter

Mean and standard deviation of relative errors (across subjects) for different T1 values (top row), mean voxel counts and outliers (middle row), and mean relative voxel content and outliers (bottom row) are shown for both dWM-mask-50-2 (left column) and dWM-mask-80-1 (right column) described in Section 3.3. Sequence: 2D-1-1800

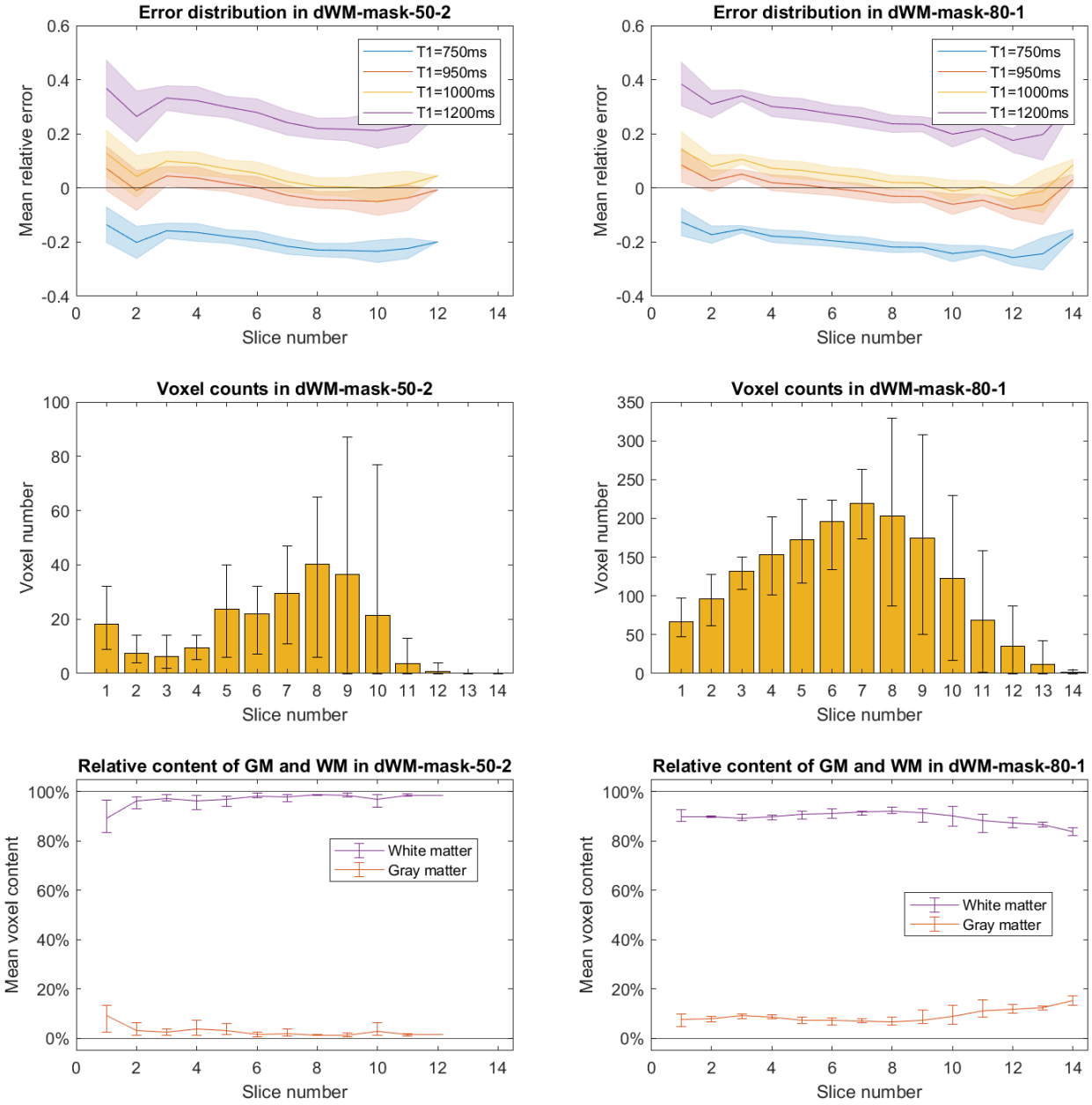

Figure 4.4: Efficiency of M0 estimation in deep WM for different T1 values in 3D GraSE in deep white matter

Mean and standard deviation of relative errors (across subjects) for different T1 values (top row), mean voxel counts and outliers (middle row), and mean relative voxel content and outliers (bottom row) are shown for both dWM-mask-50-2 (left column) and dWM-mask-80-1 (right column) described in Section 3.3. Sequence: 3D-1-1800

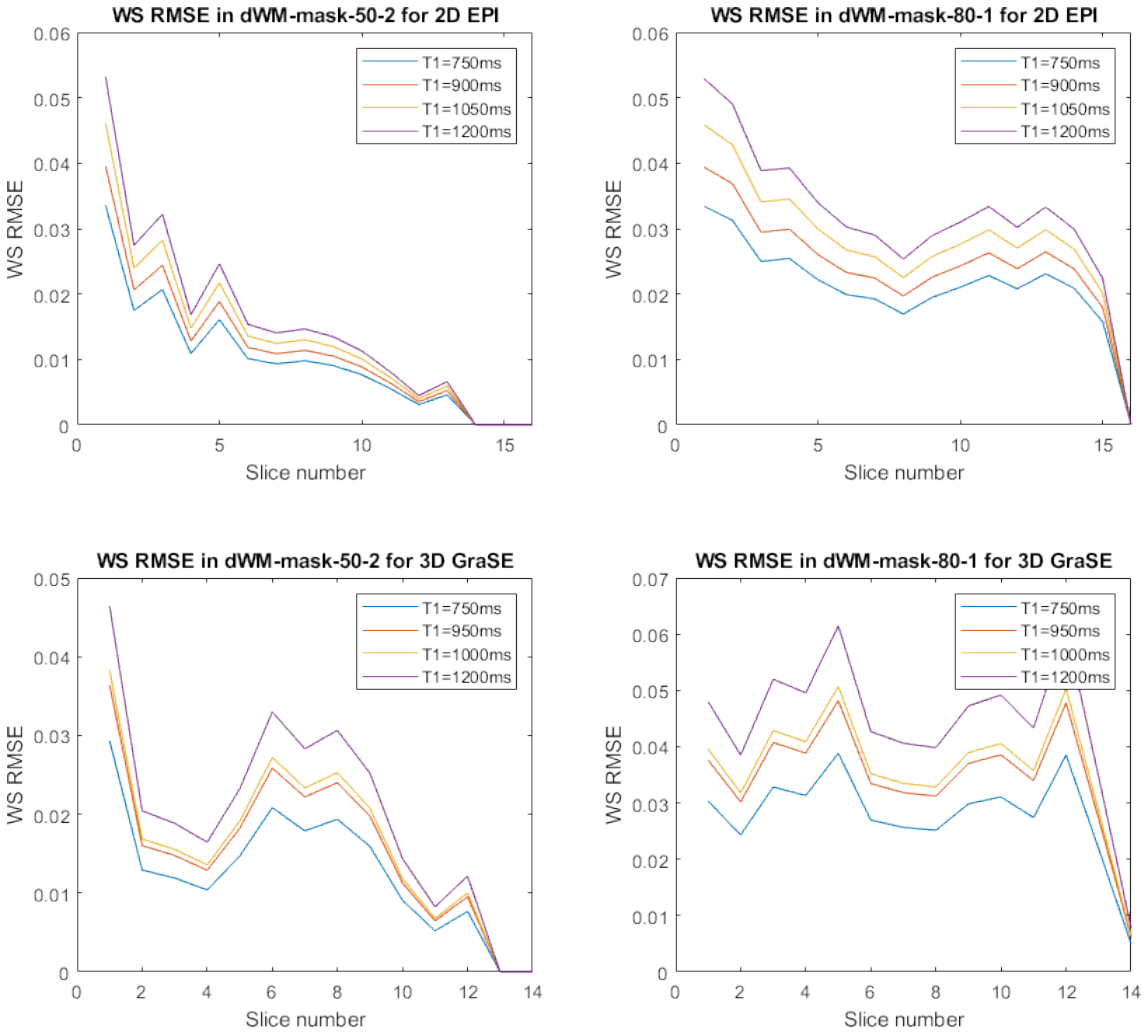

Figure 4.5: Within-subject differences in M0 estimation from controls in 2D EPI and 3D GraSE in deep WM

Mean WS RMSE (across subjects) for different T1 values are shown for both dWM-mask-50-2 (left column) and dWM-mask-80-1 (right columns) described in Section 3.3 in 2D EPI (top row) and 3D GraSE (bottom row). Sequence: 2D-1-1800, 2D-2-1800, 3D-1-1800, 3D-2-1800

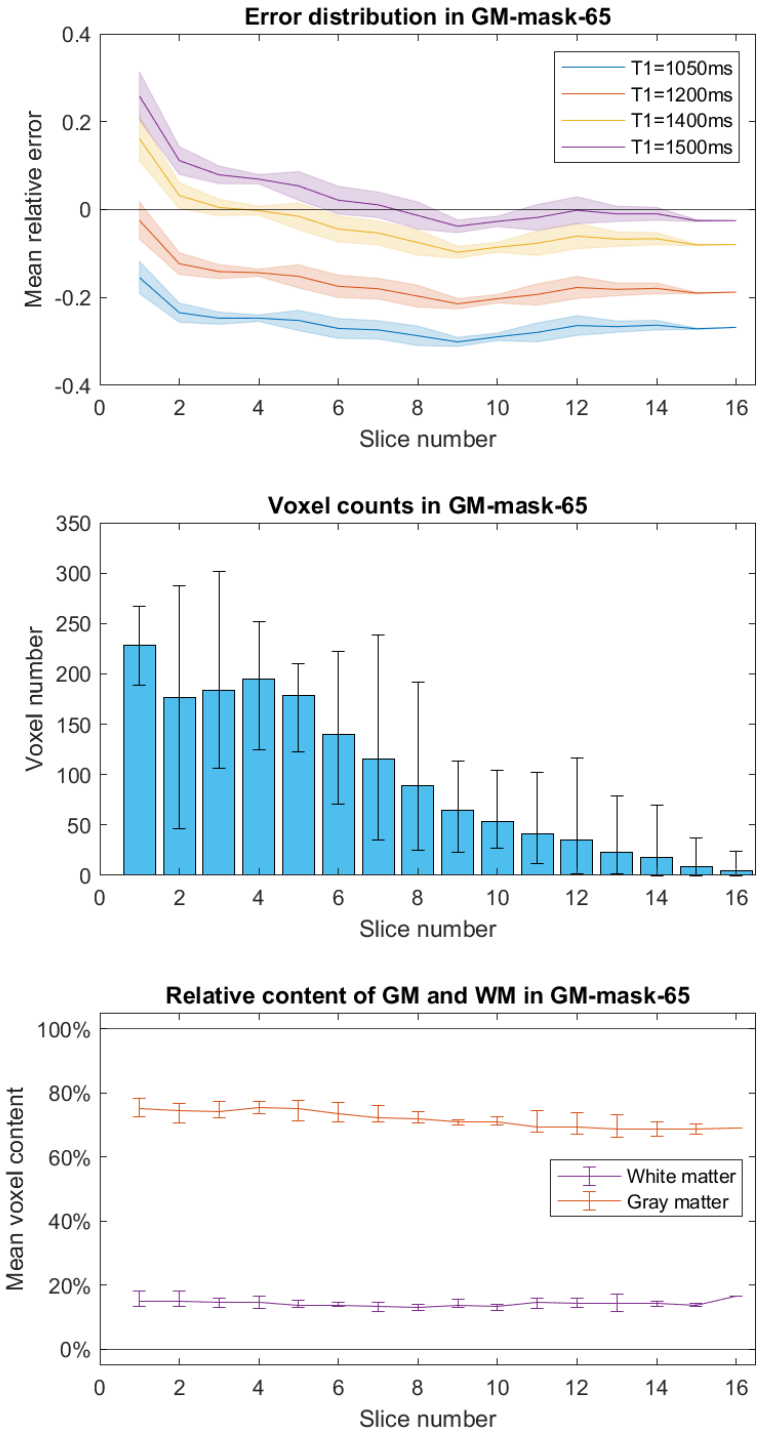

Figure 4.6: Efficiency of M0 estimation in gray matter for different T1 values in 2D EPI in gray matter

Mean and standard deviation of relative errors (across subjects) for different T1 values (top row), mean voxel counts and outliers (middle row), and mean relative voxel content and outliers (bottom row) are shown for 2D EPI for GM-mask-65 described in Section 3.3. Sequence: 2D-1-1800

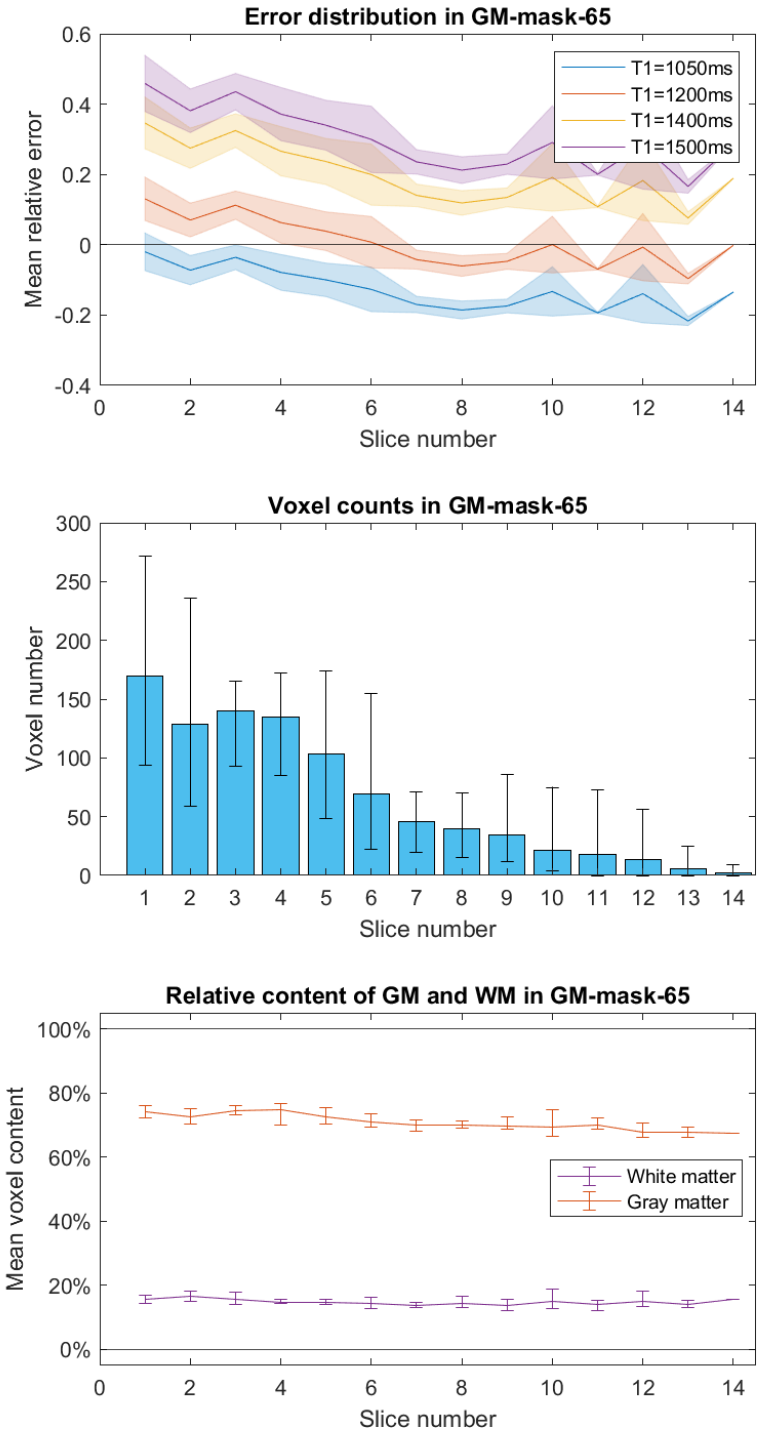

Figure 4.7: Efficiency of M0 estimation in GM for different T1 values in 3D GraSE in gray matter

Mean and standard deviation of relative errors (across subjects) for different T1 values (top row), mean voxel counts and outliers (middle row), and mean relative voxel content and outliers (bottom row) are shown for 3D GraSE for GM-mask-65 described in Section 3.3. Sequence: 3D-1-1800

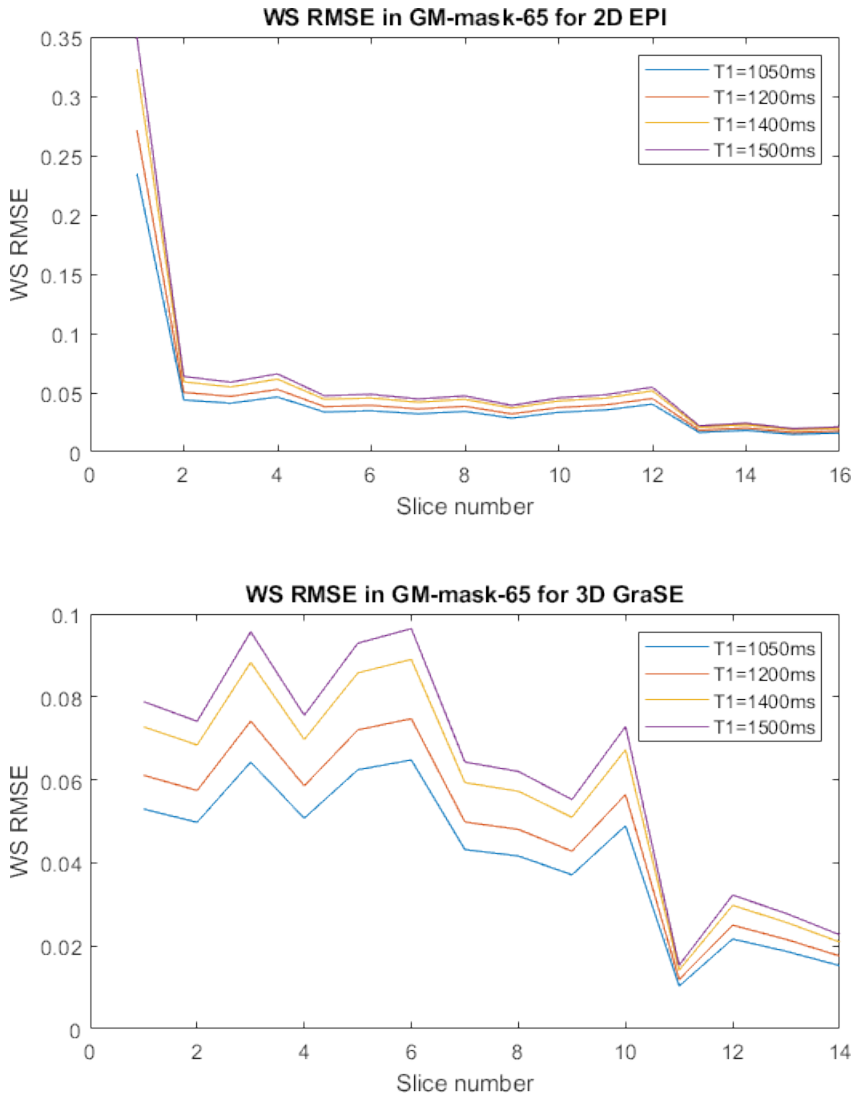

Figure 4.8: Within-subject differences in M0 estimation from controls in 2D EPI and 3D GraSE in gray matter

Mean WS RMSE (across subjects) for different T1 values are shown for GM-mask-65 described in Section 3.3 in 2D EPI (top row) and 3D GraSE (bottom row). Sequence: 2D-1-1800, 2D-2-1800, 3D-1-1800, 3D-2-1800

Using a single T1 value for BS suppression was only suboptimal for separate white and gray matters. In 2D EPI data, higher mean content of WM compared to GM led to the slightly arched curve in RME in slices 6-12, but the effect was minimal and proved our previous observations of lower optimal T1 value of white matter.

Figure 4.11 depicts the WS variance of RME estimation in the WMGM-mask-80. The WS RMSE values were higher due to the presence of both WM and GM. The higher difference of voxel number was explained by the overall greater number of voxels in WMGM-mask-80. Evidently, the WS variation in the voxel content was higher for 2D EPI. In 2D EPI, WS RMSE values for the optimal T1 = 1200 ms were below 7% across all slices. In 3D GraSE, WS RMSE values for the optimal T1 = 1050 ms were below 10% across all slices.

To better study the spatial error distribution across the slices when applying a signal BS scheme over the whole brain, the MRE distribution in 2D EPI and 3D GraSE is shown in Figures 4.12 and 4.13 respectively. In 2D EPI, compared to 3D GraSE, the MRE scores were spatially tissue-specific.

4.5 PV Correction

The accuracy of the M0 estimation with PV correction is visualized in Figures 4.14 and 4.15 for 2D EPI and 3D GraSE respectively. The T1 values used for PV correction for separate WM and GM signal correction were chosen based on the lowest MRE in the previous experiments in deep WM and GM. In 2D EPI, WM T1 value used was 1050 ms, for GM - 1500 ms; for 3D GraSE, WM T1 used was 950 ms, for GM - 1200.

For 2D EPI, the average absolute MRE across subjects in slices 4-13 was below 8% in GM with std^{MRE}_{slices} of 3.05%. In deep WM, the average absolute MRE across subjects in slices 4-13 was below 8% with std^{MRE}_{slices} of 4.17%. In whole brain, the average absolute MRE across subjects in slices 4-13 was below 4.3% with std^{MRE}_{slices} of 2.19%.

For 3D GraSE, the average absolute MRE across subjects in slices 2-12 was below 17% in GM with std^{MRE}_{slices} of 10.23%. In deep WM, the average absolute MRE across subjects in slices 2-12 was below 6% with std^{MRE}_{slices} of 4.35%. In whole brain, the average absolute MRE across subjects in slices 4-13 was below 12% with std^{MRE}_{slices} of 6.28%.

The slice-wise comparison in 2D EPI (Figure 4.16) and 3D GraSE (Figure 4.19) revealed that with PV approach (assuming different T1 values of GM and WM), the effect of the tissue differentiation of the error distribution decreased. The accuracy of the PV approach was better seen in the central slices in the Figures 4.18 and 4.19. Evidently, the method failed in the most inferior slices, but better eliminated the effect of tissue-specific longitudinal magnetization in the central slices.

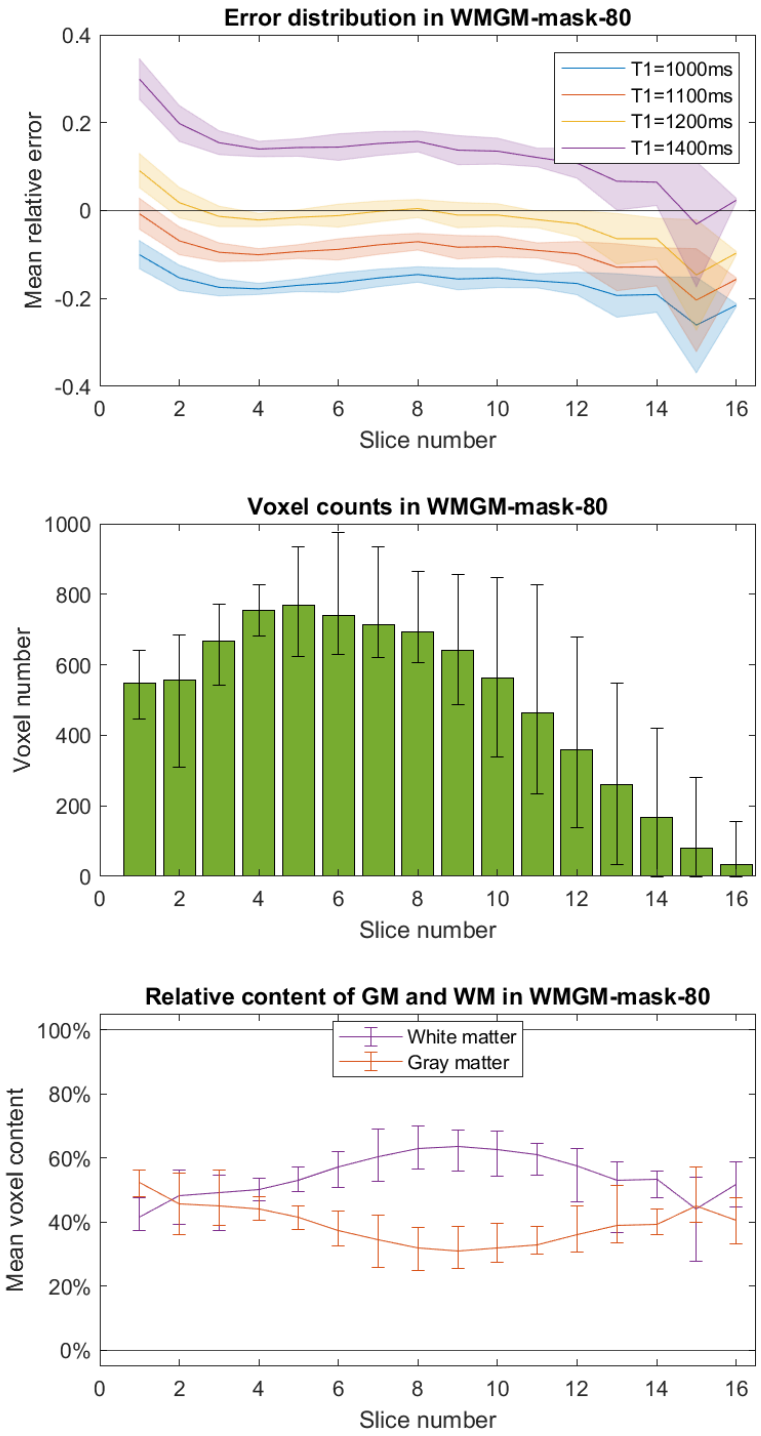

Figure 4.9: Efficiency of M0 estimation for different T1 values in 2D EPI in WMGM-mask-80

Mean and standard deviation of relative errors (across subjects) for different T1 values (top row), mean voxel counts and outliers (middle row), and mean relative voxel content and outliers (bottom row) are shown for WMGM-mask-80 described in Section 3.3. Sequence: 2D-1-1800

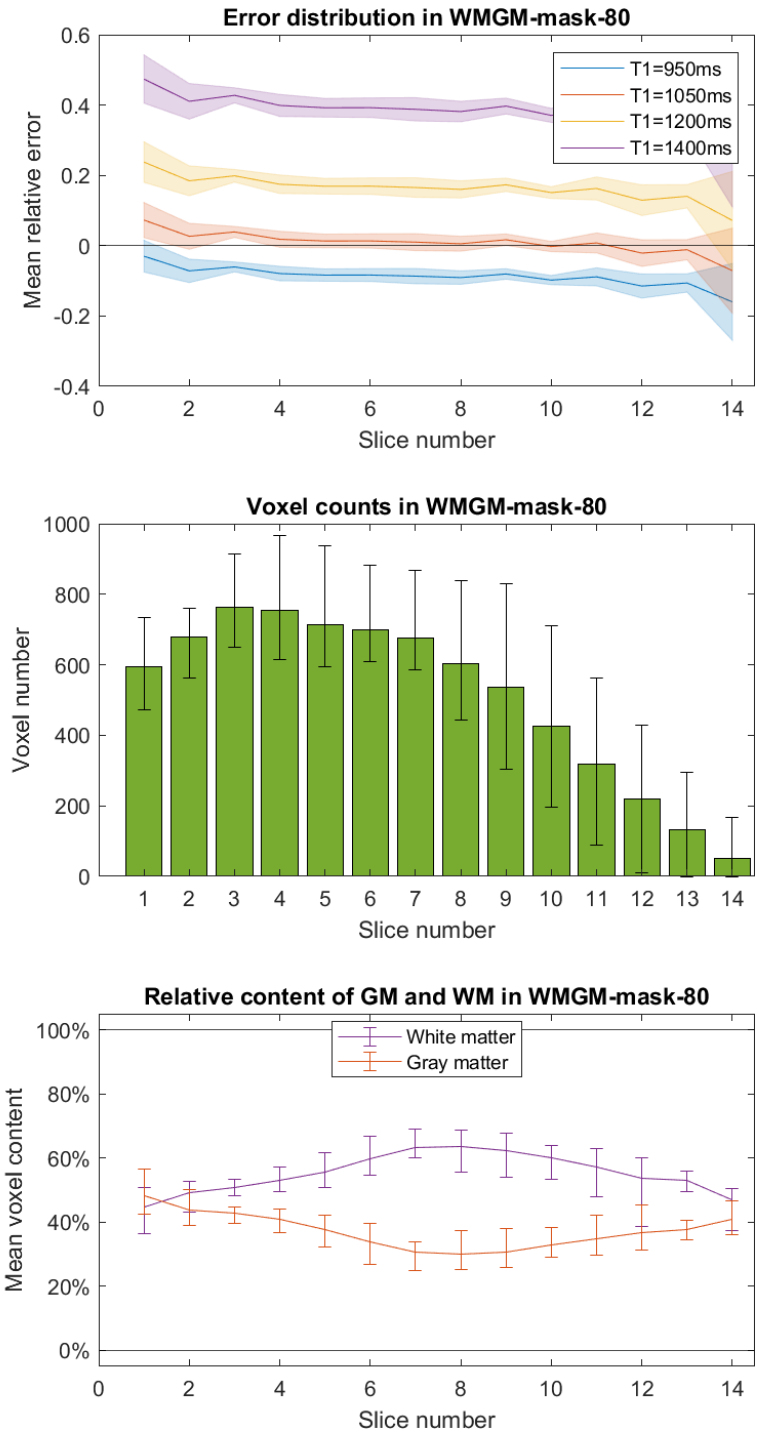

Figure 4.10: Efficiency of M0 estimation for different T1 values in 3D GraSE in WMGM-mask-80

Mean and standard deviation of relative errors (across subjects) for different T1 values (top row), mean voxel counts and outliers (middle row), and mean relative voxel content and outliers (bottom row) are shown for WMGM-mask-80 described in Section 3.3. Sequence: 3D-1-1800

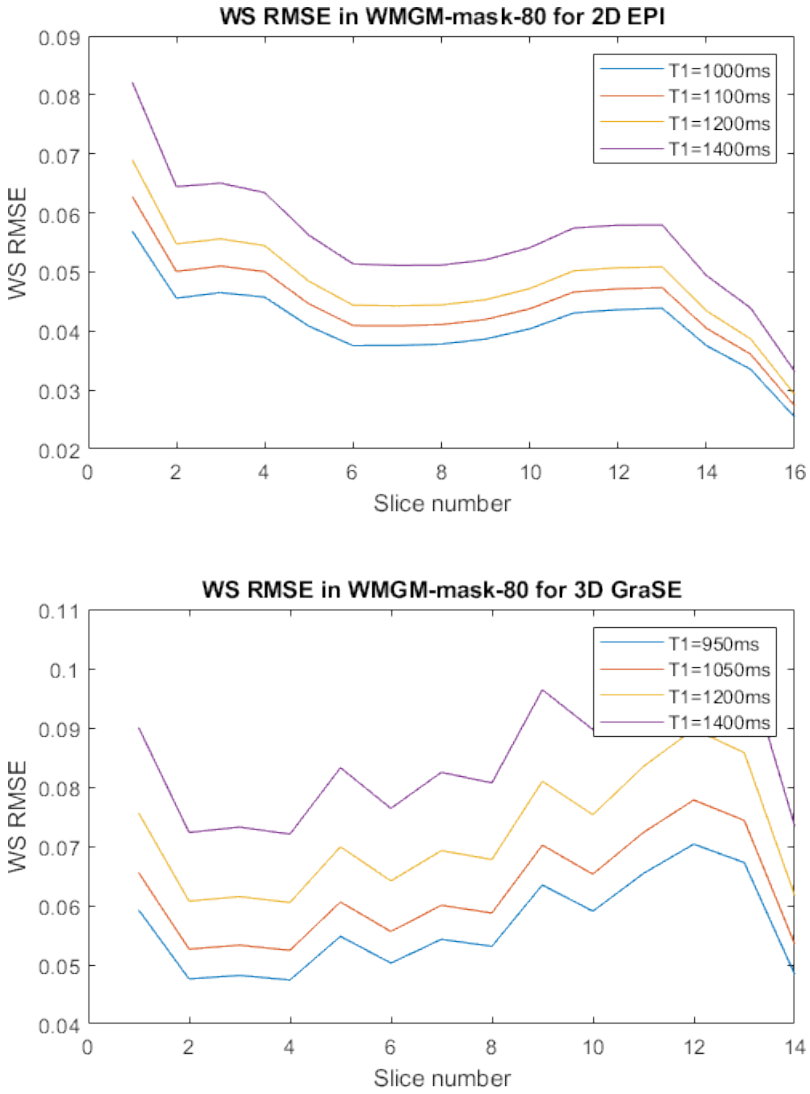

Figure 4.11: Within-subject differences in M0 estimation from controls in 2D EPI and 3D GraSE in WMGM-mask-80

Mean WS RMSE (across subjects) for different T1 values are shown for WMGM-mask-80 described in Section 3.3 in 2D EPI (top row) and 3D GraSE (bottom row). Sequence: 2D-1-1800, 2D-2-1800, 3D-1-1800, 3D-2-1800

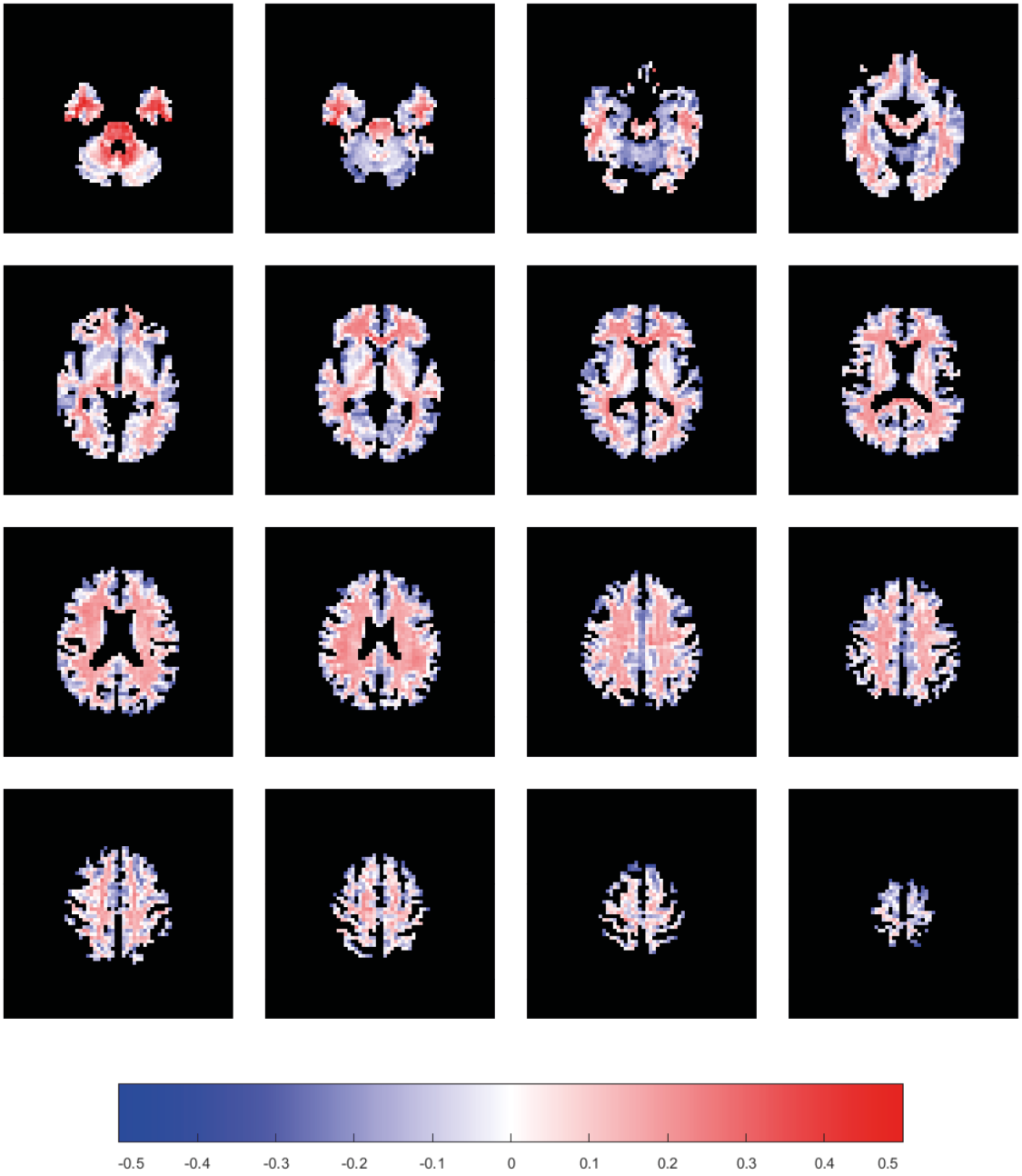

Figure 4.12: Spatial error distribution of M0 estimation with single-tissue model for T1 = 1200 ms in WMGM-mask-80 in 2D EPI)
Sequence: 2D-1-1800, Subject: V04S02

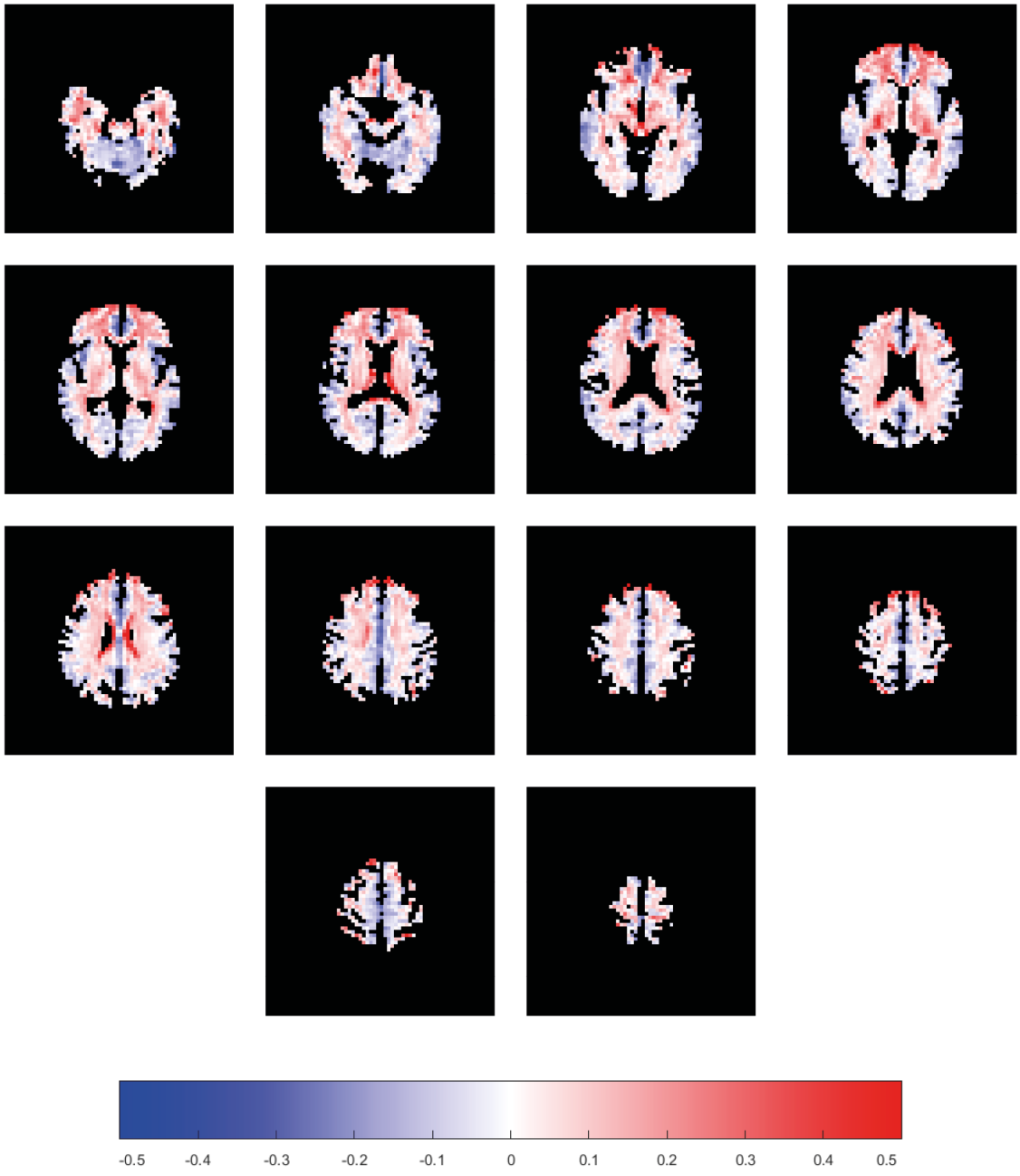

Figure 4.13: Spatial error distribution of M0 estimation with single-tissue model for T1 = 1050 ms in WMGM-mask-80 in 3D GraSE
Sequence: 3D-1-1800, Subject V04S02

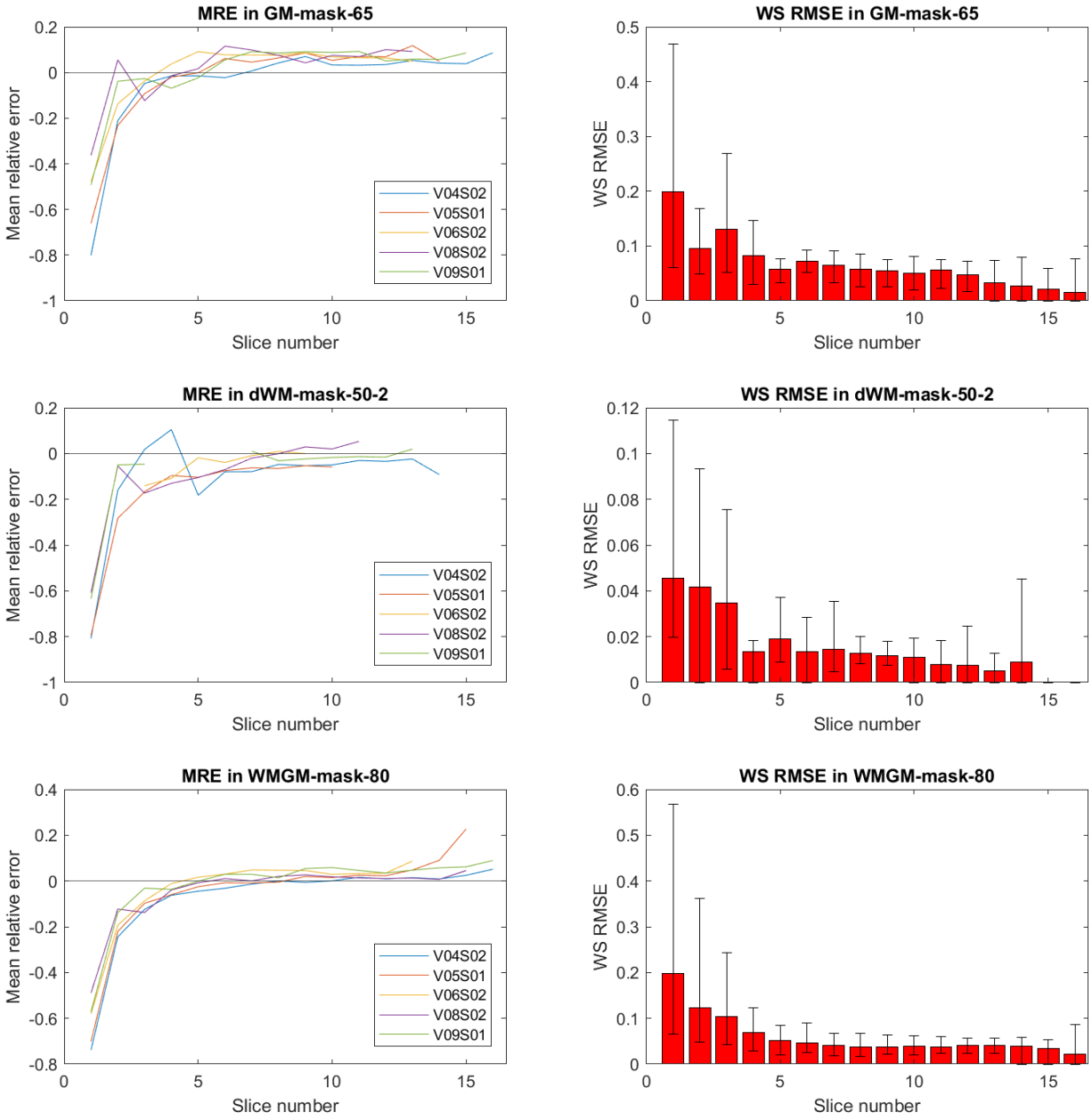

Figure 4.14: Accuracy of M0 estimation using PV correction in 2D EPI data
Sequence: 2D-1-1800, T1(WM) = 1050 ms, T1(GM) = 1500 ms

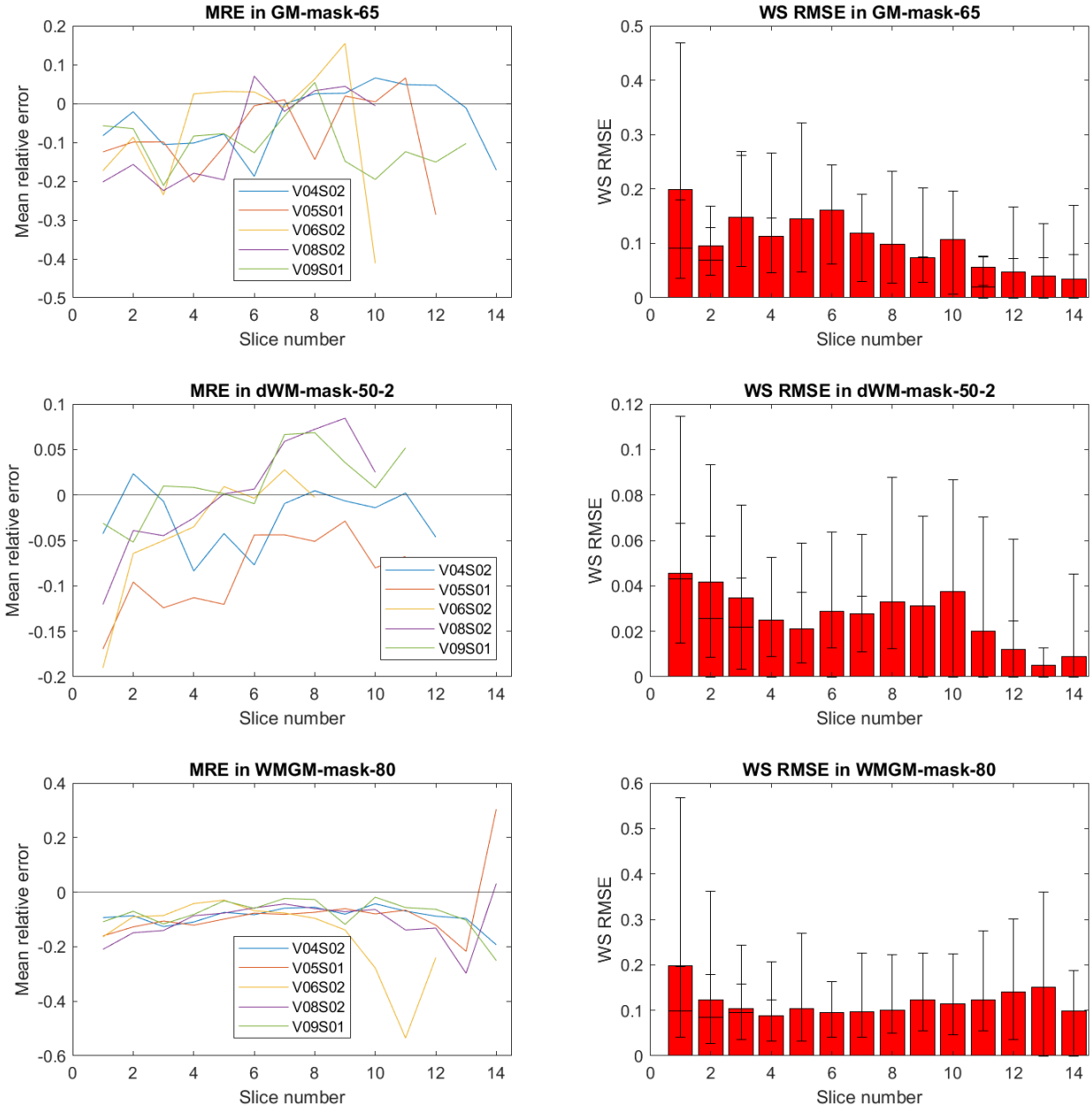

Figure 4.15: Accuracy of M0 estimation using PV correction in 3D GraSE data
Sequence: 3D-1-1800, T1(WM) = 950 ms, T1(GM) = 1200 ms

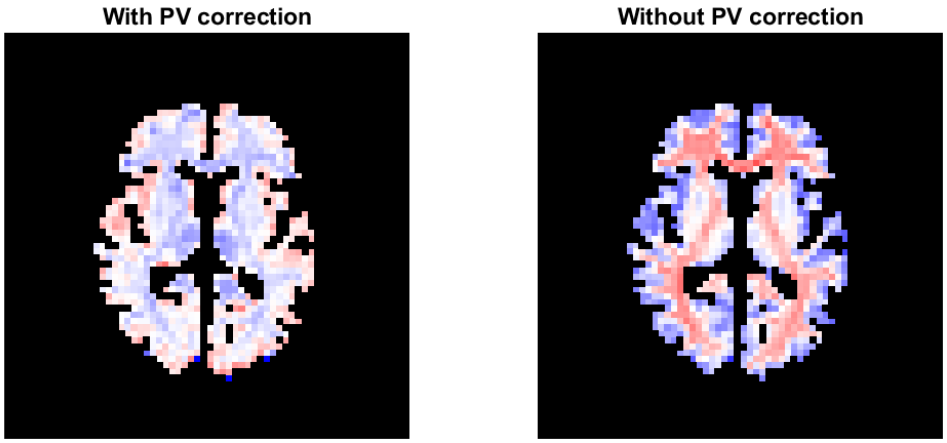

Figure 4.16: Comparison of M0 estimation assuming different T1 values for GM and WM (PVC) and assuming single T1 value for the whole brain (without PVC) in 2D EPI
Sequence: 2D-1-1800, Subject: V04S02, Slice: 7

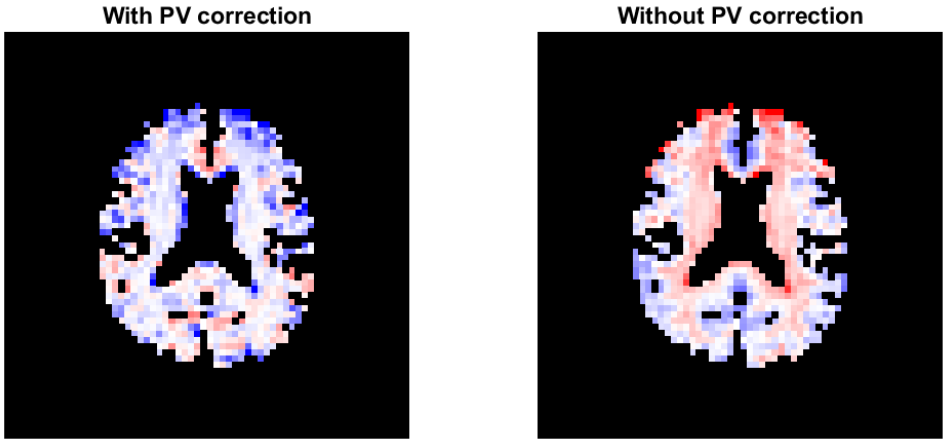

Figure 4.17: Comparison of M0 estimation assuming different T1 values for GM and WM (PVC) and assuming single T1 value for the whole brain (without PVC) in 3D GraSE
Sequence: 3D-1-1800, Subject: V04S02, Slice: 7

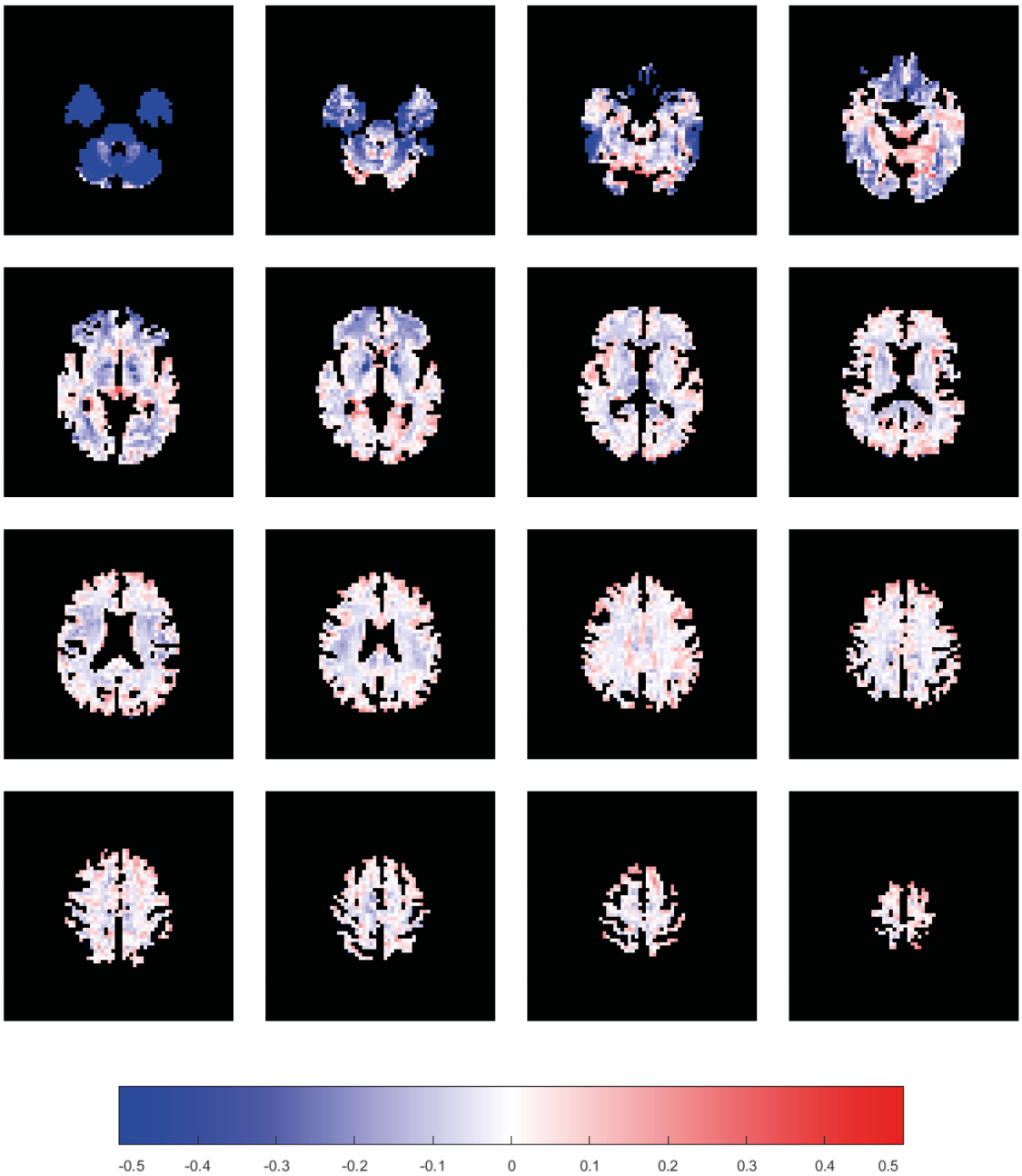

Figure 4.18: Spatial distribution of errors in M0 estimation with PVC in 2D EPI
Sequence: 2D-1-1800, Subject: V04S02

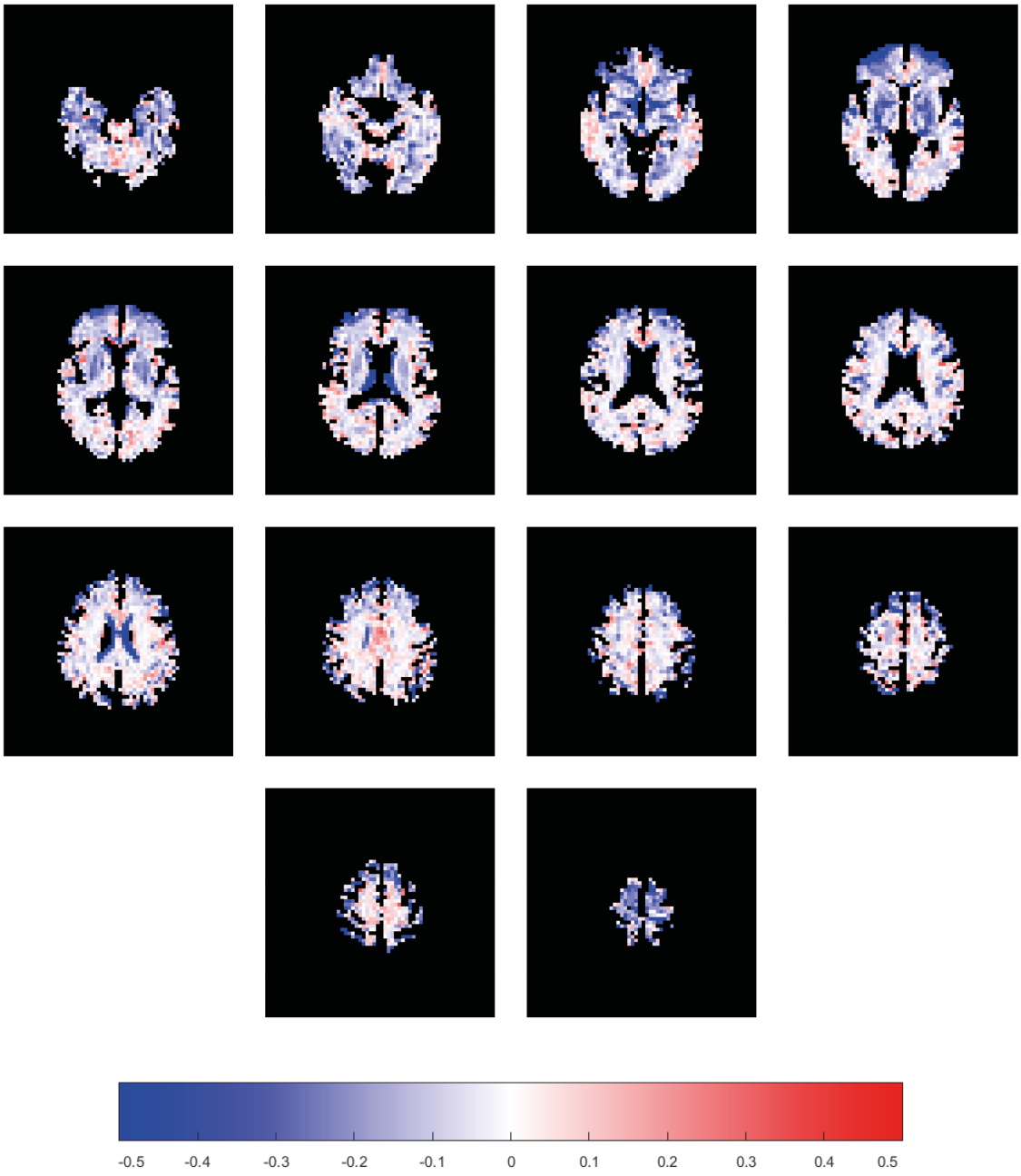

Figure 4.19: Spatial distribution of errors in M0 estimation with PVC in 3D GraSE Sequence: 3D-1-1800, Subject: V04S02

4.6 Validation in CBF quantification

Results for the quantified CBF from the estimated M0 images with and without PV approach in 2D EPI and 3D GraSE are visualized in the Figures 4.20 - 4.23. With PV correction, absolute MRE was below 10% in slices 4-11 for the whole brain, in slices 4-12 in GM, and in slice 5-11 in deep WM for all subjects. The WS RMSE in PV method fell below expected 6.7% in slices 4-14 in the whole brain, in slices 4-16 in GM, and in slices 1-13 in deep WM [60]. The std^{MRE}_{slices} and $std^{MRE}_{subjects}$ are reported in Table 4.1.

The accuracy of estimated CBF in 2D EPI without PVC was lower compared to the accuracy of estimated CBF with PVC method. The absolute MRE fell below 10% only for some subjects in whole brain and WM. The absolute MRE in GM was more than 10% for all subjects and slices. Moreover, WS RMSE values were higher than the expected CBF CoV in whole brain (slices 1-6), GM (slices 1-4, 7-8), and WM (slices 3-5). The results for stability in slices and subjects are reported in the Table 4.2. The variation in MRE among slices was lower or comparable to the results of the PV approach, but between-subject variation was higher.

ROI	std^{MRE}_{slices}	$std^{MRE}_{subjects}$
Whole brain	5.12%	1.61%
Gray matter	3.66%	2.3%
Deep white matter	5.95%	2.44%

Table 4.1: Stability of MRE in estimated CBF with PV approach in 2D EPI

ROI	std^{MRE}_{slices}	$std^{MRE}_{subjects}$
Whole brain	3.44%	6.9%
Gray matter	1.85%	5.64%
Deep white matter	6.71%	8.26%

Table 4.2: Stability of MRE in estimated CBF without PV approach in 2D EPI

For 3D GraSE, the PV approach led to the average MRE below 10% for slices 2-10 in whole brain, for slices 2-11 in GM, and for all slices in deep WM (Figure 4.22). Values of WS RMSE were below the expected CBF CoV in slices 2-7 in whole brain, in slices 2-14 in GM, and slices 2-5, 9-12 in deep WM.

The results for calculated CBF without the PV approach were comparable in values to those derived from the PV method. The mean absolute MRE values were below 10% in slices 1-9 in whole brain, in slices 1-6 in GM, and 1-10 in deep WM.

Finally, t-tests revealed a significant difference between the true and quantified CBF using M0 image in all subjects in 2D EPI without PV correction, in 3 subjects in 2D EPI with PV correction, in 4 subjects in 3D GraSE without PV correction, and in 3 subjects with the PV correction (Table 4.5).

ROI	std^{MRE}_{slices}	$std^{MRE}_{subjects}$
Whole brain	7.7%	4.24%
Gray matter	5.59%	4.22%
Deep white matter	4.26%	3.59%

Table 4.3: Stability of MRE in estimated CBF with PV approach in 3D GraSE

ROI	std^{MRE}_{slices}	$std^{MRE}_{subjects}$
Whole brain	6.34%	5.23%
Gray matter	5.09%	5.23%
Deep white matter	3.19%	2.49%

Table 4.4: Stability of MRE in estimated CBF without PV approach in 3D GraSE

Subject	2D EPI		3D GraSE	
	CBF_{ref} VS CBF^{PV}_{est}	CBF_{ref} VS CBF^{nonPV}_{est}	CBF_{ref} VS CBF^{PV}_{est}	CBF_{ref} VS CBF^{nonPV}_{est}
V04S02	5.1e-6	0	0.26	7.1e-10
V05S01	0.46	1.1e-13	1.1e-6	0.12
V06S02	0.053	8.5e-17	0.59	6.9e-19
V08S02	0.017	1.6e-15	4.4e-8	6.3e-20
V09S01	2.4e-6	0	1.1e-4	1.9e-14

Table 4.5: p-values obtained from t-tests comparing reference and estimated CBF
Estimated CBF was calculated from the estimated M0 with and without PVC

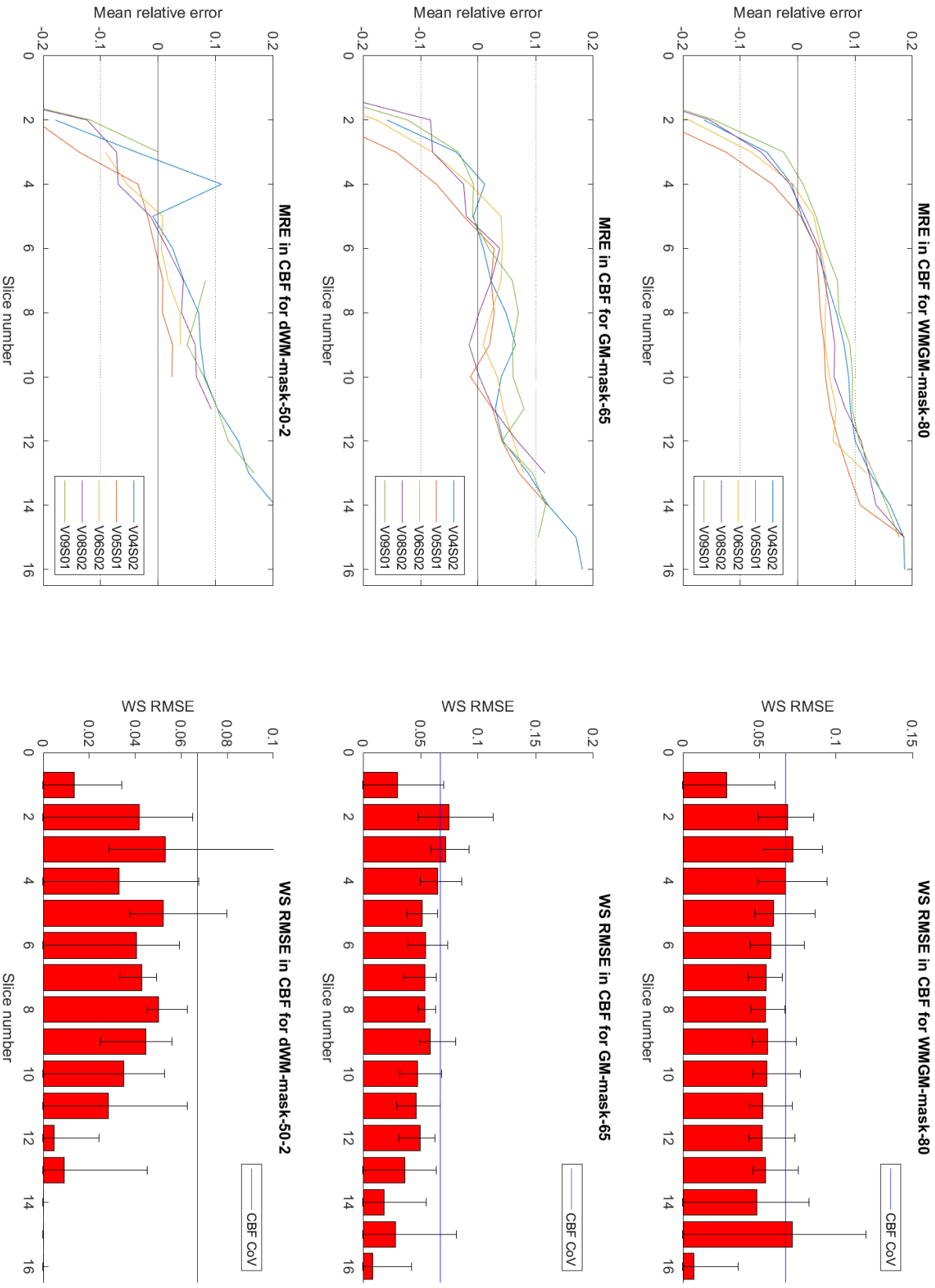

Figure 4.20: PV correction accuracy in resulting CBF in 2D EPI Experiment: 2D-1-1800, 2D-2-1800

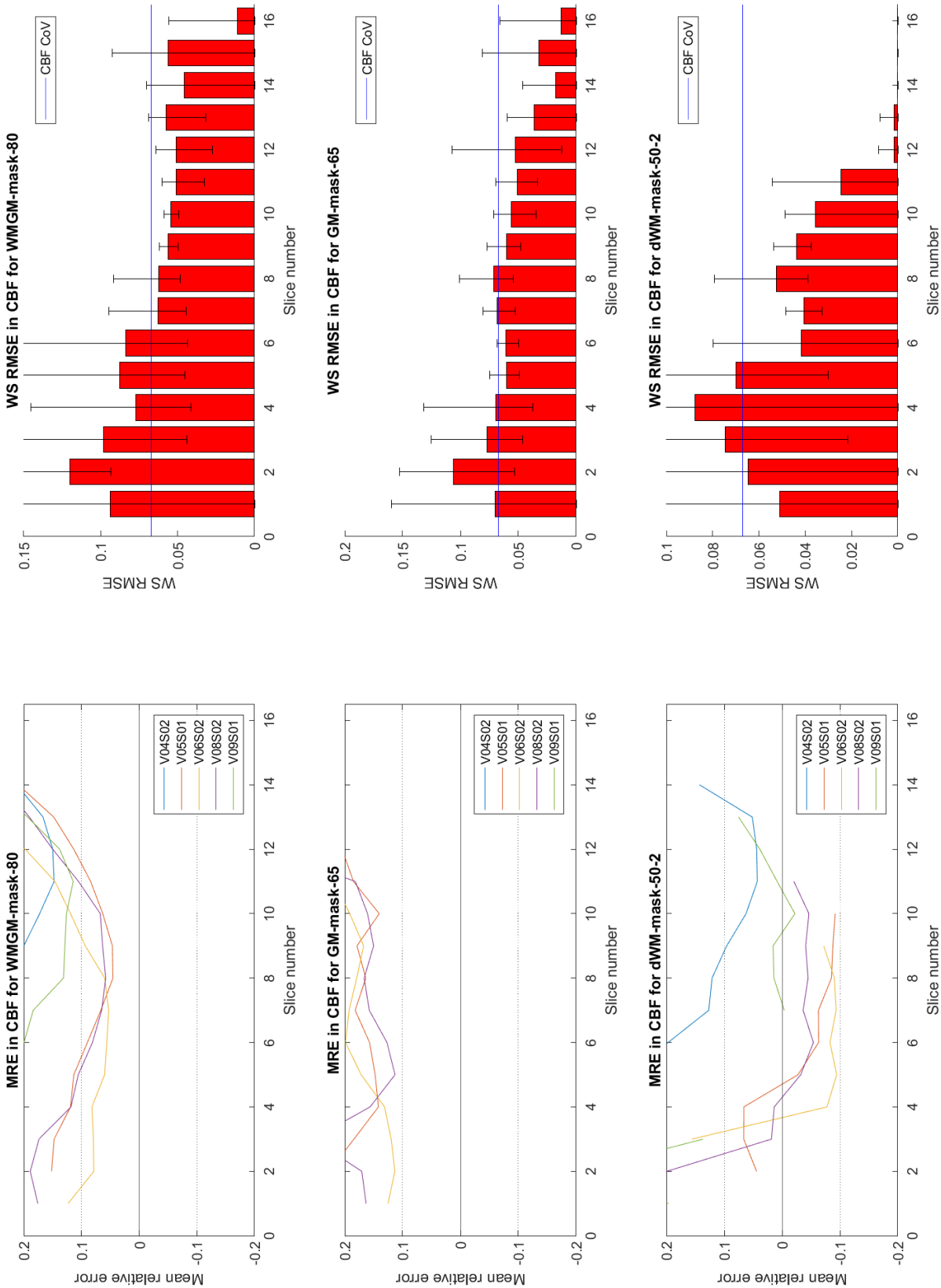

Figure 4.21: BS correction without PV approach accuracy in resulting CBF in 2D EPI Experiment: 2D-1-1800, 2D-2-1800

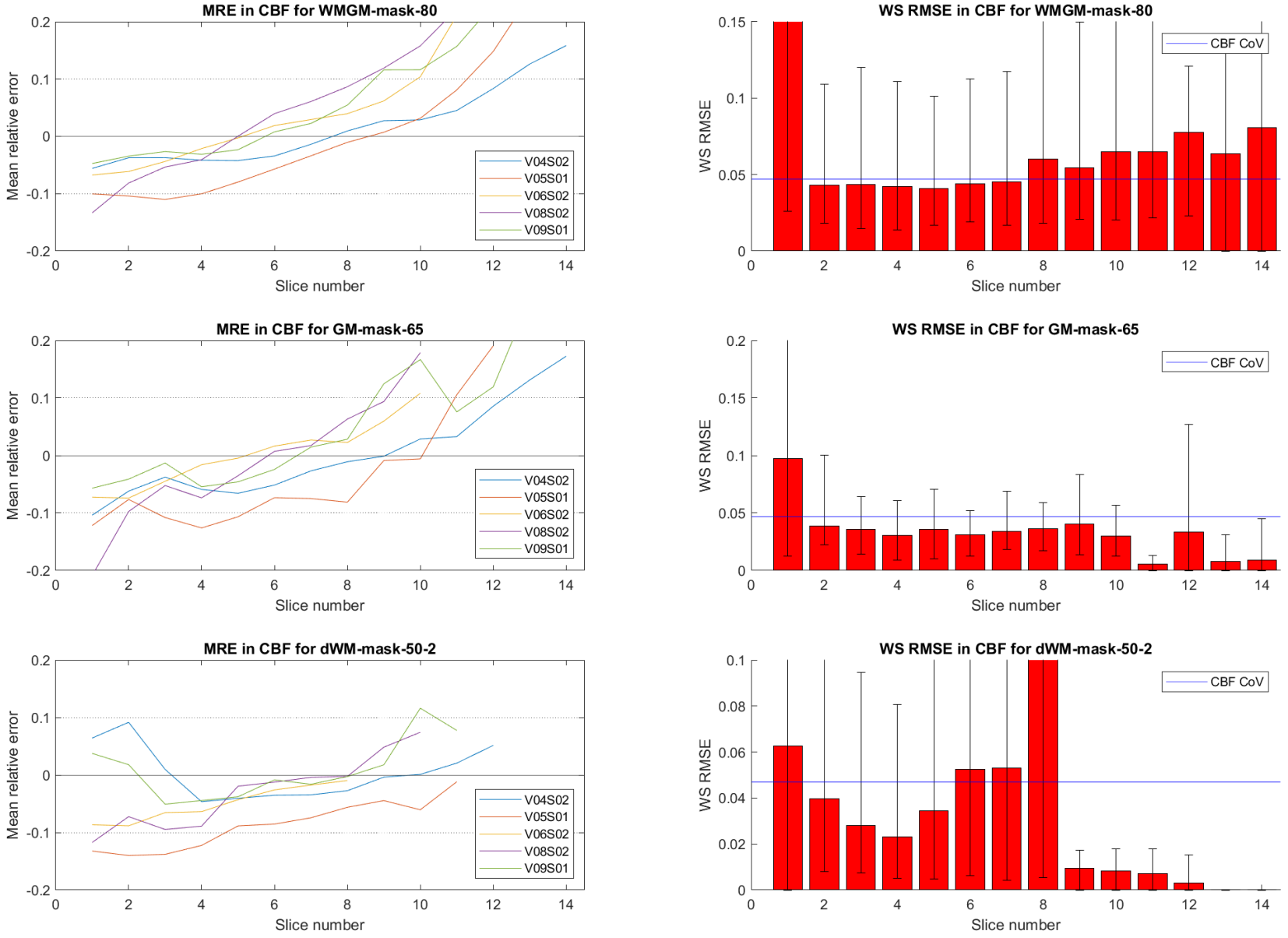

Figure 4.22: PV correction accuracy in resulting CBF in 3D GraSE
Experiment: 3D-1-1800, 3D-2-1800

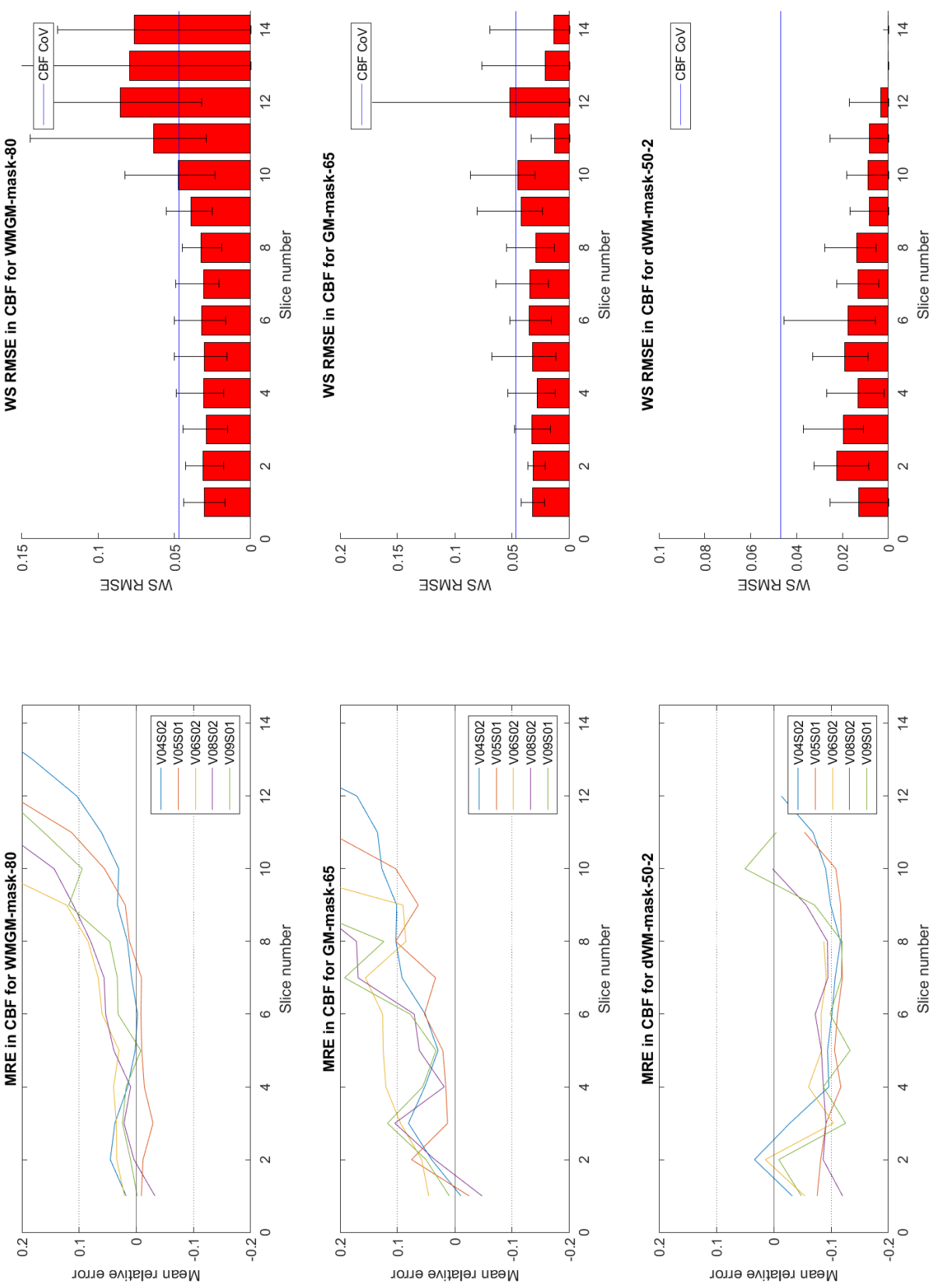

Figure 4.23: BS correction without PV approach accuracy in resulting CBF in 3D GraSE Experiment: 3D-1-1800, 3D-2-1800

Chapter 5

Discussion

Arterial spin labeling (ASL) is a method for magnetic resonance imaging (MRI) that allows to measure brain perfusion non-invasively using magnetically labeled water instead of using radioactive tracers or contrast agents. Its main advantages are fast measurement time suitable for clinical use, ability to provide stable absolute quantification of perfusion, and a complete non-invasivness. To obtain absolute quantification, the value of equilibrium magnetization in arterial blood needs to be obtained in every patient. This is usually done with the use of a so-called M0 scan that can be rapidly obtained along with the ASL measurement. Despite the acquisition of an M0-scan is recommended in the majority of literature, it is not always available in practice. There is an important base of clinical studies that either omitted the M0-scan acquisition, acquired it with incorrect parameters, or lost the data during data curation. This work aims to provide the necessary tools for absolute perfusion quantification also in these cases by using the signal from ASL images with background suppression (BS).

The modeling of signal changes caused by the background suppression in ASL has been previously investigated in the literature, however, background-suppression correction was not yet employed to M0-image estimation for the purpose of ASL quantification. The idea proposed in this thesis is to model the background suppression scheme to derive the M0 image. Since static tissue in the brain consists of GM and WM with different magnetization properties, the background suppression correction was also adjusted to the tissue differentiation for the partial volume effect. Two main approaches were tested in this work to estimate the M0 image from the control scans with background suppression. The simpler approach estimates the M0 image assuming a single T1 value for the whole brain (single tissue approach). A more complex solution is to correct for BS and reconstruct an M0 image while assuming different T1 values in WM and GM and possible mixing of the GM and WM signals in each voxel (mixed tissue approach). Performance of both methods was evaluated by comparing the estimated M0 images with a real acquired reference M0 scan. The difference between the estimated and reference M0 was evaluated in terms of accuracy (using MRE parameter) and within-subject and between-session reproducibility (using WS RMSE parameter). Validation of the methods was done by quantifying CBF

using the estimated M0 images (both with single tissue and mixed tissue approaches) and comparing it with reference CBF calculated from the true acquired M0 scan.

The initial data exploration (Section 4.1) showed the discrepancies in signals between 2D EPI and 3D GraSE readoutes both in the control images and in the M0 images (Figure 4.1). In 2D EPI control scans, the signal rises towards the superior slices, which is an expected behavior for this type of imaging given the loss of BS efficiency due to T1 relaxation in time for 2D multi-slice sequences (Figure 2.2). Control scans of 3D GraSE showed a different trend with only a slight decrease of the signal in the superior slices. This is due to the fact that the BS efficiency is homogeneous for the whole 3D volume in the single-excitation 3D readouts. The slight signal decrease across slices can be explained by structural changes in tissue composition in the brain and is visible in the M0 scans without BS as well. Another difference between 2D EPI and 3D GraSE is the signal variation in GM and WM. 2D EPI showed visible contrast between signal in WM and GM both in control with BS, whereas GM and WM difference was only minimal in 3D GraSE. This is partly because the perfect BS in 3D sequences and partly because of higher blurring typical for 3D GraSE readouts [63]. Taken together, due to higher contrast between GM and WM, PVC is expected to yield higher benefit in the 2D EPI readout.

Afterwards, the optimal T1 values were investigated for the single-tissue model. This was studied in four different ROI to take into account the spatial distribution of different tissues: two masks for deep WM, one mask for GM, and a whole brain mask. Two masks for WM were used to elicit the challenge of creating a mask that is large enough to guarantee stability with noisy data while decreasing the influence of signal contamination from other tissues - even though WM structure is relatively thick, correct masking is still an issue given the low resolution of ASL images. dWM-mask-50-2 contained voxels with almost unique content of WM and thus more favorable accuracy in estimation, however, it had a low number of voxels, which complicated its usage in practice in extremal slices 4.3. dWM-mask-80-1 had a larger number of voxels at a cost of 10% GM contamination, which potentially biases the M0 image estimation towards GM. In the case of GM-mask-65 and WMGM-mask-80, a reasonable tradeoff was difficult to achieve and to avoid contamination by signal from different tissue showing the need to use of PVC and mixed-tissue model 4.6.

The optimal derived T1 values for WM and GM were 1050 ms (absolute MRE below 6% for central slices in M0-image estimation) and 1500 ms (absolute MRE below 8% in central slices) in 2D EPI and 950 ms (absolute MRE below 6% for central slices) and 1200 ms (absolute MRE below 12% in central slices) in 3D GraSE. The results differ from the literature T1 values for GM (1445 ms) and for WM (791 ms) [64], probably due to the possible PVE in the maps and low resolution. The derived optimal T1 values were lower for 3D GraSE supposedly due fact that the resolution is slightly lower than in the 2D EPI readout due to the higher T2* contrast and blurring in the in-place phase-enconding direction [65]. The absolute MRE values were higher for GM because GM mask was less homogeneous when it comes to tissue distribution and had more important tissue mixing.

In WMGM-mask-80, the single-tissue model of the brain showed optimal T1 values 1200 ms and 1050 ms in 2D EPI and 3D GraSE respectively (for both, absolute MRE values were below 5% for both readouts). However, the visualization of the spatial error

distribution in the Figures 4.12 and 4.13 shows tissue differentiation - positive errors were located in WM areas, whereas negative errors were located in the GM, which was further addressed by the mixed-tissue model. With the PVC method, absolute MRE values were below 5% for WMGM-mask-80 and below 12% for 2D EPI and 3D GraSE respectively. The visualizations of the spatial error distribution (Figures 4.18, 4.19) show that there is a smaller effect of tissue location. The estimation error in 3D GraSE was higher probably due to the smaller signal differentiation per tissue in the control scans, which is supported by the previous observations.

Both methods for M0-image estimation were incorporated into the ExploreASL pipeline to show their performance in CBF quantification and to compare them with CBF estimation using the true acuqired M0 scan. For 2D EPI data, mixed-tissue model improved the CBF calculation comparing to the single-tissue model both in terms of accuracy and reproducibility of the results. The best results were achieved in the central slices (absolute MRE below 8% with WS RMSE below 10%). The accuracy and reproducibility were worse in most inferior and superior slices probably due to the structure of the brain - lower amount of voxels in the masks lead to inaccurate BS correction. In mixed-tissue model, absolute MRE was within 10% for central slices for all subjects in all ROI, whereas in single-tissue model, the absolute MRE was above 10% in some subjects and ROI (in GM, MRE was above 10% in all slices and subjects). Comparing to single-tissue model, the mixed-tissue method improved the between-subject variation of CBF accuracy (1.61-2.44% in mixed-tissue method and 5.64-8.26% in single-tissue method) with comparable variation in slices (3.66-5.95% with PVC compared to 1.85-6.71% without PVC). Such a difference can be explained by the loss of BS efficiency in higher slices, leading to higher signal difference in WM and GM due to different T1 values. The accuracy and reproducibility are comparable to within-subject CoV of this type of imaging, described in the study by Baas et al. [60]. The mixed-tissue approach has proven to improve M0 estimation that led to CBF results with sufficient accuracy and reproducibility comparing to the reported WS CoV of 6.7% for 2D EPI.

The difference between the mixed- and single-tissue approaches was less evident in 3D GraSE than in 2D EPI data due to the difference in image acquisition explained above. Mean absolute MRE values were below 10% for the central slices for both single tissue and mixed tissue approach approach, but the CBF accuracy was better in WM and GM with using PVC (absolute MRE within 10% for all subjects) comparing to the estimation without PVC (MRE above 10% for selected subjects in GM and WM). Both MRE variation in slices (4.26-7.7% for mixed tissue approach and 3.59-4.24% for single tissue approach) and in subjects (3.19-6.34% for mixed tissue approach and 2.49-5.23% for single tissue approach) are comparable for both methods. In 3D GraSE, both PVC and non-PVC approaches showed sufficient accuracy and reproducibility in both estimation of M0 and resulting CBF comparing to the reported WS CoV of 4.7% [60].

5.1 Limitations and future perspectives

CBF quantification directly uses equilibrium magnetization of blood ($M0_{0b}$). This is commonly derived from the equilibrium magnetization of tissue (M_{0t}), which can be extracted from an M0 scan. The conversion from M_{0t} to $M0_{0b}$ is conventionally done using brain-blood partition coefficient, which differs in GM and WM. However, for simplification, a GM model is assumed in the whole brain as the usual focus is on CBF quantification in GM. In this work, we have tested several methods for M_{0t} estimation from control images with BS and we have taken into account the differences in GM and WM. However, our main focus was the restoration of the M0-scan (M_{0t}) and for the final quantification step of M_{0b} and CBF calculation, we used the standard way of using a GM model only. While this has no influence on our results and conclusions concerning M0-scan estimation, using a two tissue model also for the last step of CBF quantification can lead to a better CBF quantification and should be studied in the future following the method by Pinto et al. [23].

Second limitation is a relatively small sample size. While the data allowed us to study these effects in two typical readout sequences and also establish the repeatability of this approach, using the full population from the study by Baas et al. [60] should be done in the future. While higher statistical power will be gained, we do not expect that the conclusions or results will be affected. The current subsample of the study population included only participants from the age range of 46-80y. The performance of the method thus needs to be ascertained also in the rest of the population containing younger subjects. Final limitation related to the study population is that fact that data were obtained in healthy volunteers only. While presence of pathology will influence the T1 times and the quality of the BS correction, adverse effects on the CBF quantification are not expected as the calculation of blood M0 has to be done anyway in healthy tissue only and a presence of pathologies is a complication for the whole calibration process, irrespective of the source of M0 scans. Lastly, the dataset was acquired in Philips scanner with 4 given BS pulses, the methods' accuracy has to be additionally tested in other scanners with different readouts, different number of BS pulses and different BS pulse timings.

A further limitation lies in the process of selecting optimal T1 values. The WM masks were selected in mostly pure WM, however, there was a large contamination of WM signal on the GM mask. The derived optimal T1-values were thus optimal in the sense of working with the given amount of tissue signal contamination. However, it effectively prevented us from confirming the performance with literature T1-values or finding out the correct individual values. This probably had a negative effect on the mixed-model estimation of the M0-scan as true tissue T1 values are supposed to be used for the mixed-model.

All the aforementioned issues are planned to be addressed in future work. We plan to use the full dataset provided by Baas et al. [60] to study the performance of the method in both young and older subjects of a sufficiently large population. We will investigate the accuracy also in several other datasets with different readout type and readout parameters. We will study the effect of M_{0b} estimation from M0-scan M_{0t} to gain the complex picture of use of control images with BS on CBF quantification. Lastly, we will investigate in

more details the effect of optimal T1-time for each tissue. We will directly optimize the PV approach for BS correction in order to find the optimal set of T1-times rather than probing optimizing it on potentially contaminated masks. We will study further sequence details that might have an effect on the optimal T1-times and modeling of BS correction as specific BS efficiency and B1-field inhomogeneities.

5.2 Conclusion

This work proposes a novel approach to M0 scan estimation from the background-suppressed control scans acquired during ASL imaging. It shows that such an approach is theoretically possible with a reasonable error in final CBF quantification compared with the use of true acquired M0 scans and that the between-session reproducibility of this approach is very high both in 2D EPI and 3D GraSE sequences. Moreover, the results show that the use of a PVC-based approach (assuming a mixed-tissue model) further improves the M0-scan estimation and offers a suitable solution for practical use in quantification of CBF data from ASL acquisition with background suppression and without a dedicated M0-scan, thus opening the possibility to re-analyze several large clinical studies.

Bibliography

[1] Buxton, R. B.; Frank, L. R. A model for the coupling between cerebral blood flow and oxygen metabolism during neural stimulation. *Journal of cerebral blood flow & metabolism*, volume 17, no. 1, 1997: pp. 64–72.

[2] Geiger, A. Correlation of brain metabolism and function by the use of a brain perfusion method in situ. *Physiological Reviews*, volume 38, no. 1, 1958: pp. 1–20.

[3] Coelho-Filho, O. R.; Rickers, C.; Kwong, R. Y.; et al. MR myocardial perfusion imaging. *Radiology*, volume 266, no. 3, 2013: pp. 701–715.

[4] Zhang, J. L.; Lee, V. S. Renal perfusion imaging by MRI. *Journal of Magnetic Resonance Imaging*, volume 52, no. 2, 2020: pp. 369–379.

[5] Chouhan, M. D.; Ramasawmy, R.; Bainbridge, A.; et al. Liver perfusion MRI in a rodent model of cirrhosis: Agreement with bulk-flow phase-contrast MRI and noninvasive evaluation of inflammation in chronic liver disease using flow-sensitive alternating inversion recovery arterial spin labelling and tissue T1. *NMR in Biomedicine*, 2020: p. e4423.

[6] Khanal, S.; Turnbull, P. R.; Vaghefi, E.; et al. Repeatability of arterial spin labeling MRI in measuring blood perfusion in the human eye. *Journal of Magnetic Resonance Imaging*, volume 49, no. 4, 2019: pp. 966–974.

[7] Winkel, D. J.; Heye, T. J.; Benz, M. R.; et al. Compressed sensing radial sampling MRI of prostate perfusion: utility for detection of prostate cancer. *Radiology*, volume 290, no. 3, 2019: pp. 702–708.

[8] Telischak, N. A.; Detre, J. A.; Zaharchuk, G. Arterial spin labeling MRI: clinical applications in the brain. *Journal of Magnetic Resonance Imaging*, volume 41, no. 5, 2015: pp. 1165–1180.

[9] Staffaroni, A. M.; Cobigo, Y.; Elahi, F. M.; et al. A longitudinal characterization of perfusion in the aging brain and associations with cognition and neural structure. *Human brain mapping*, volume 40, no. 12, 2019: pp. 3522–3533.

[10] Brown, R. K.; Bohnen, N. I.; Wong, K. K.; et al. Brain PET in suspected dementia: patterns of altered FDG metabolism. *Radiographics*, volume 34, no. 3, 2014: pp. 684–701.

[11] Heron, C. J. L.; Wright, S. L.; Melzer, T. R.; et al. Comparing cerebral perfusion in Alzheimer's disease and Parkinson's disease dementia: an ASL-MRI study. *Journal of Cerebral Blood Flow & Metabolism*, volume 34, no. 6, 2014: pp. 964–970.

[12] Taylor, J.-P.; Firbank, M. J.; He, J.; et al. Visual cortex in dementia with Lewy bodies: magnetic resonance imaging study. *The British Journal of Psychiatry*, volume 200, no. 6, 2012: pp. 491–498.

[13] Dehkharghani, S.; Andre, J. Imaging approaches to stroke and neurovascular disease. *Neurosurgery*, volume 80, no. 5, 2017: pp. 681–700.

[14] Lapointe, E.; Li, D.; Traboulsee, A.; et al. What have we learned from perfusion MRI in multiple sclerosis? *American Journal of Neuroradiology*, volume 39, no. 6, 2018: pp. 994–1000.

[15] Hirai, T.; Kitajima, M.; Nakamura, H.; et al. Quantitative blood flow measurements in gliomas using arterial spin-labeling at 3T: intermodality agreement and inter-and intraobserver reproducibility study. *American Journal of Neuroradiology*, volume 32, no. 11, 2011: pp. 2073–2079.

[16] Stephens, J. A.; Liu, P.; Lu, H.; et al. Cerebral blood flow after mild traumatic brain injury: associations between symptoms and post-injury perfusion. *Journal of neurotrauma*, volume 35, no. 2, 2018: pp. 241–248.

[17] Ota, M.; Kanie, A.; Kobayashi, Y.; et al. Pseudo-continuous arterial spin labeling MRI study of patients with obsessive–compulsive disorder. *Psychiatry Research: Neuroimaging*, 2020: p. 111124.

[18] Cooper, C. M.; Fatt, C. R. C.; Liu, P.; et al. Discovery and replication of cerebral blood flow differences in major depressive disorder. *Molecular psychiatry*, volume 25, no. 7, 2020: pp. 1500–1510.

[19] Yerys, B. E.; Herrington, J. D.; Bartley, G. K.; et al. Arterial spin labeling provides a reliable neurobiological marker of autism spectrum disorder. *Journal of Neurodevelopmental Disorders*, volume 10, no. 1, 2018: p. 32.

[20] Tomandl, B. F.; Klotz, E.; Handschu, R.; et al. Comprehensive imaging of ischemic stroke with multisection CT. *Radiographics*, volume 23, no. 3, 2003: pp. 565–592.

[21] Erdoğan, M. A.; Apaydin, M.; Armagan, G.; et al. Evaluation of toxicity of gadolinium-based contrast agents on neuronal cells. *Acta Radiologica*, 2020: p. 0284185120920801.

[22] Petersen, E.; Zimine, I.; Ho, Y. L.; et al. Non-invasive measurement of perfusion: a critical review of arterial spin labelling techniques. *The British journal of radiology*, volume 79, no. 944, 2006: pp. 688–701.

[23] Pinto, J.; Chappell, M. A.; Okell, T. W.; et al. Calibration of arterial spin labeling data—potential pitfalls in post-processing. *Magnetic resonance in medicine*, volume 83, no. 4, 2020: pp. 1222–1234.

[24] Sabati, M.; Maudsley, A. A. Fast and high-resolution quantitative mapping of tissue water content with full brain coverage for clinically-driven studies. *Magnetic resonance imaging*, volume 31, no. 10, 2013: pp. 1752–1759.

[25] McGehee, B. E.; Pollock, J. M.; Maldjian, J. A. Brain perfusion imaging: how does it work and what should I use? *Journal of magnetic resonance imaging*, volume 36, no. 6, 2012: pp. 1257–1272.

[26] Petcharunpaisan, S.; Ramalho, J.; Castillo, M. Arterial spin labeling in neuroimaging. *World journal of radiology*, volume 2, no. 10, 2010: p. 384.

[27] Alsop, D. C.; Detre, J. A. Reduced transit-time sensitivity in noninvasive magnetic resonance imaging of human cerebral blood flow. *Journal of Cerebral Blood Flow & Metabolism*, volume 16, no. 6, 1996: pp. 1236–1249.

[28] Alsop, D. C.; Detre, J. A. Background suppressed 3D RARE ASL perfusion imaging. *International Society for Magnetic Resonance in Medicine. Philadelphia*, 1999: p. 601.

[29] Ye, F. Q.; Frank, J. A.; Weinberger, D. R.; et al. Noise reduction in 3D perfusion imaging by attenuating the static signal in arterial spin tagging (ASSIST). *Magnetic Resonance in Medicine: An Official Journal of the International Society for Magnetic Resonance in Medicine*, volume 44, no. 1, 2000: pp. 92–100.

[30] Dai, W.; Garcia, D.; De Bazelaire, C.; et al. Continuous flow-driven inversion for arterial spin labeling using pulsed radio frequency and gradient fields. *Magnetic Resonance in Medicine: An Official Journal of the International Society for Magnetic Resonance in Medicine*, volume 60, no. 6, 2008: pp. 1488–1497.

[31] Mutsaerts, H. J.; Petr, J.; Groot, P.; et al. ExploreASL: an image processing pipeline for multi-center ASL perfusion MRI studies. *NeuroImage*, 2020: p. 117031.

[32] Alsop, D. C.; Detre, J. A.; Golay, X.; et al. Recommended implementation of arterial spin-labeled perfusion MRI for clinical applications: a consensus of the ISMRM perfusion study group and the European consortium for ASL in dementia. *Magnetic resonance in medicine*, volume 73, no. 1, 2015: pp. 102–116.

[33] Ferré, J.-C.; Bannier, E.; Raoult, H.; et al. Arterial spin labeling (ASL) perfusion: techniques and clinical use. *Diagnostic and interventional imaging*, volume 94, no. 12, 2013: pp. 1211–1223.

[34] Mutsaerts, H. J.; van Osch, M. J.; Zelaya, F. O.; et al. Multi-vendor reliability of arterial spin labeling perfusion MRI using a near-identical sequence: implications for multi-center studies. *Neuroimage*, volume 113, 2015: pp. 143–152.

[35] Heijtel, D. F.; Mutsaerts, H. J.; Bakker, E.; et al. Accuracy and precision of pseudo-continuous arterial spin labeling perfusion during baseline and hypercapnia: a head-to-head comparison with 15O H2O positron emission tomography. *Neuroimage*, volume 92, 2014: pp. 182–192.

[36] Deibler, A.; Pollock, J.; Kraft, R.; et al. Arterial spin-labeling in routine clinical practice, part 1: technique and artifacts. *American Journal of Neuroradiology*, volume 29, no. 7, 2008: pp. 1228–1234.

[37] Wong, E. C. Quantifying CBF with pulsed ASL: technical and pulse sequence factors. *Journal of Magnetic Resonance Imaging: An Official Journal of the International Society for Magnetic Resonance in Medicine*, volume 22, no. 6, 2005: pp. 727–731.

[38] Wong, E. C.; Buxton, R. B.; Frank, L. R. A theoretical and experimental comparison of continuous and pulsed arterial spin labeling techniques for quantitative perfusion imaging. *Magnetic resonance in medicine*, volume 40, no. 3, 1998: pp. 348–355.

[39] Grade, M.; Tamames, J. H.; Pizzini, F.; et al. A neuroradiologist's guide to arterial spin labeling MRI in clinical practice. *Neuroradiology*, volume 57, no. 12, 2015: pp. 1181–1202.

[40] Han, P. K.; Choi, S. H.; Park, S.-H. Investigation of control scans in pseudo-continuous arterial spin labeling (p CASL): Strategies for improving sensitivity and reliability of p CASL. *Magnetic resonance in medicine*, volume 78, no. 3, 2017: pp. 917–929.

[41] Mutsaerts, H. J.; Petr, J.; Václav, L.; et al. The spatial coefficient of variation in arterial spin labeling cerebral blood flow images. *Journal of Cerebral Blood Flow & Metabolism*, volume 37, no. 9, 2017: pp. 3184–3192.

[42] Mansfield, P. Multi-planar image formation using NMR spin echoes. *Journal of Physics C: Solid State Physics*, volume 10, no. 3, 1977: p. L55.

[43] Stehling, M. K.; Turner, R.; Mansfield, P. Echo-planar imaging: magnetic resonance imaging in a fraction of a second. *Science*, volume 254, no. 5028, 1991: pp. 43–50.

[44] Feinberg, D. A.; Oshio, K. GRASE (gradient-and spin-echo) MR imaging: a new fast clinical imaging technique. *Radiology*, volume 181, no. 2, 1991: pp. 597–602.

[45] Günther, M.; Oshio, K.; Feinberg, D. A. Single-shot 3D imaging techniques improve arterial spin labeling perfusion measurements. *Magnetic Resonance in Medicine: An Official Journal of the International Society for Magnetic Resonance in Medicine*, volume 54, no. 2, 2005: pp. 491–498.

[46] Wong, E. C.; Cronin, M.; Wu, W.-C.; et al. Velocity-selective arterial spin labeling. *Magnetic Resonance in Medicine: An Official Journal of the International Society for Magnetic Resonance in Medicine*, volume 55, no. 6, 2006: pp. 1334–1341.

[47] Garcia, D. M.; Duhamel, G.; Alsop, D. C. Efficiency of inversion pulses for background suppressed arterial spin labeling. *Magnetic Resonance in Medicine: An Official Journal of the International Society for Magnetic Resonance in Medicine*, volume 54, no. 2, 2005: pp. 366–372.

[48] Shao, X.; Wang, Y.; Moeller, S.; et al. A constrained slice-dependent background suppression scheme for simultaneous multislice pseudo-continuous arterial spin labeling. *Magnetic resonance in medicine*, volume 79, no. 1, 2018: pp. 394–400.

[49] Donahue, M. J.; Lu, H.; Jones, C. K.; et al. An account of the discrepancy between MRI and PET cerebral blood flow measures. A high-field MRI investigation. *NMR in Biomedicine: An International Journal Devoted to the Development and Application of Magnetic Resonance In vivo*, volume 19, no. 8, 2006: pp. 1043–1054.

[50] Asllani, I.; Borogovac, A.; Brown, T. R. Regression algorithm correcting for partial volume effects in arterial spin labeling MRI. *Magnetic Resonance in Medicine: An Official Journal of the International Society for Magnetic Resonance in Medicine*, volume 60, no. 6, 2008: pp. 1362–1371.

[51] Petr, J.; Mutsaerts, H. J.; De Vita, E.; et al. Effects of systematic partial volume errors on the estimation of gray matter cerebral blood flow with arterial spin labeling MRI. *Magnetic Resonance Materials in Physics, Biology and Medicine*, volume 31, no. 6, 2018: pp. 725–734.

[52] Buxton, R. B.; Frank, L. R.; Wong, E. C.; et al. A general kinetic model for quantitative perfusion imaging with arterial spin labeling. *Magnetic resonance in medicine*, volume 40, no. 3, 1998: pp. 383–396.

[53] Zhao, M. Y.; Václav, L.; Petersen, E. T.; et al. Quantification of cerebral perfusion and cerebrovascular reserve using Turbo-QUASAR arterial spin labeling MRI. *Magnetic resonance in medicine*, volume 83, no. 2, 2020: pp. 731–748.

[54] Li, Y.; Liu, P.; Li, Y.; et al. ASL-MRICloud: An online tool for the processing of ASL MRI data. *NMR in Biomedicine*, volume 32, no. 2, 2019: p. e4051.

[55] Shirzadi, Z.; Stefanovic, B.; Chappell, M. A.; et al. Enhancement of automated blood flow estimates (ENABLE) from arterial spin-labeled MRI. *Journal of Magnetic Resonance Imaging*, volume 47, no. 3, 2018: pp. 647–655.

[56] Chappell, M. A.; Groves, A. R.; Whitcher, B.; et al. Variational Bayesian inference for a nonlinear forward model. *IEEE Transactions on Signal Processing*, volume 57, no. 1, 2008: pp. 223–236.

[57] Ashburner, J. SPM: a history. *Neuroimage*, volume 62, no. 2, 2012: pp. 791–800.

[58] Çavuşoğlu, M.; Pfeuffer, J.; Uğurbil, K.; et al. Comparison of pulsed arterial spin labeling encoding schemes and absolute perfusion quantification. *Magnetic resonance imaging*, volume 27, no. 8, 2009: pp. 1039–1045.

[59] Suzuki, Y.; Okell, T. W.; Chappell, M. A.; et al. A framework for motion correction of background suppressed arterial spin labeling perfusion images acquired with simultaneous multi-slice EPI. *Magnetic resonance in medicine*, volume 81, no. 3, 2019: pp. 1553–1565.

[60] Baas, K.; Petr, J.; Kuijer, J.; et al. Effects of Acquisition Parameter Modifications and Field Strength on the Reproducibility of Brain Perfusion Measurements Using Arterial Spin-Labeling. *American Journal of Neuroradiology*, volume 42, no. 1, 2021: pp. 109–115.

[61] Gaser, C. Partial volume segmentation with adaptive maximum a posteriori (MAP) approach. *NeuroImage*, , no. 47, 2009: p. S121.

[62] Mutsaerts, H. J.; Richard, E.; Heijtel, D. F.; et al. Gray matter contamination in arterial spin labeling white matter perfusion measurements in patients with dementia. *NeuroImage: Clinical*, volume 4, 2014: pp. 139–144.

[63] Boland, M.; Stirnberg, R.; Pracht, E. D.; et al. Accelerated 3D-GRASE imaging improves quantitative multiple post labeling delay arterial spin labeling. *Magnetic resonance in medicine*, volume 80, no. 6, 2018: pp. 2475–2484.

[64] Chen, L.; Bernstein, M.; Huston, J.; et al. Measurements of T1 relaxation times at 3.0 T: implications for clinical MRA. In *Proceedings of the 9th Annual Meeting of ISMRM, Glasgow, Scotland*, 2001.

[65] Kemper, V. G.; De Martino, F.; Vu, A. T.; et al. Sub-millimeter T2 weighted fMRI at 7 T: comparison of 3D-GRASE and 2D SE-EPI. *Frontiers in neuroscience*, volume 9, 2015: p. 163.